

DIGITAL ACCESS TO SCHOLARSHIP AT HARVARD

Substrate stiffness regulates cadherin-dependent collective migration through myosin-II contractility

The Harvard community has made this article openly available. Please share how this access benefits you. Your story matters.

Citation	Ng, Mei Rosa, Achim Besser, Gaudenz Danuser, and Joan S. Brugge. 2012. Substrate stiffness regulates cadherin-dependent collective migration through myosin-ii contractility. The Journal of Cell Biology 199(3): 545-563.
Published Version	doi:10.1083/jcb.201207148
Accessed	February 19, 2015 12:05:42 PM EST
Citable Link	http://nrs.harvard.edu/urn-3:HUL.InstRepos:11180361
Terms of Use	This article was downloaded from Harvard University's DASH repository, and is made available under the terms and conditions applicable to Other Posted Material, as set forth at http://nrs.harvard.edu/urn-3:HUL.InstRepos:dash.current.terms-of-use#LAA

(Article begins on next page)

Substrate stiffness regulates cadherin-dependent collective migration through myosin-II contractility

Mei Rosa Ng, Achim Besser, Gaudenz Danuser, and Joan S. Brugge

Department of Cell Biology, Harvard Medical School, Boston, MA 02115

The mechanical microenvironment is known to influence single-cell migration; however, the extent to which mechanical cues affect collective migration of adherent cells is not well understood. We measured the effects of varying substrate compliance on individual cell migratory properties in an epithelial wound-healing assay. Increasing substrate stiffness increased collective cell migration speed, persistence, and directionality as well as the coordination of cell movements. Dynamic analysis revealed that wounding initiated a wave of motion coordination from the wound edge into the sheet. This was accompanied by a front-to-back gradient of myosin-II activation and establishment of cell polarity. The propagation was faster and farther reaching on stiff substrates, indicating that substrate stiffness affects the transmission of directional cues. Manipulation of myosin-II activity and cadherin–catenin complexes revealed that this transmission is mediated by coupling of contractile forces between neighboring cells. Thus, our findings suggest that the mechanical environment integrates in a feedback with cell contractility and cell–cell adhesion to regulate collective migration.

Introduction

Cells often migrate collectively as part of a group, sheet, or strand maintained by cell–cell junctions (Friedl and Gilmour, 2009; Ilina and Friedl, 2009; Rørth, 2009; Weijer, 2009). Collective migration is involved in *Dictyostelium discoideum* slug formation (Firtel and Meili, 2000), border cell migration during *Drosophila melanogaster* oogenesis (Prasad and Montell, 2007), zebrafish posterior lateral line primordium development (Revenu and Gilmour, 2009), gastrulation (Keller, 2005; Weijer, 2009), morphogenesis of organs such as mammary glands (Ewald et al., 2008, 2012) and kidney (Vasilyev et al., 2009), and reepithelialization during wound healing (Martin, 1997). Collective migration has also been observed in cancer explants in vitro (Friedl et al., 1995) and invasive tumors in vivo (Friedl et al., 2004; Hidalgo-Carcedo et al., 2011).

Within tissues, cells encounter microenvironments that may range in compliance from tens of pascals in the softest tissues, such as brain, to gigapascals in the stiffest tissues, such as bone (Discher et al., 2005; Butcher et al., 2009). Such variation in matrix mechanical properties has long been known to play a role in regulating single-cell behaviors, including migration (Pelham and Wang, 1997; Flanagan et al., 2002; Engler et al., 2004, 2006; Discher et al., 2005; Guo et al., 2006; Ingber, 2006). Sparsely seeded cells migrate from a soft to a rigid surface, a mechanoresponsiveness referred to as durotaxis (Lo et al., 2000). Microenvironmental stiffness has also been implicated in breast cancer cell invasion in vitro and metastasis in vivo (Wozniak et al., 2003; Paszek et al., 2005; Kostic et al., 2009; Levental et al., 2009), both of which may involve collective cell migration.

The effects of substrate stiffness on cell sheets may not be as significant as those on single cells. Studies using polyacrylamide (PAA) gel–based substrates have shown that the differences in cell spreading area observed in single fibroblasts and endothelial cells cultured on soft versus stiff substrates disappeared once the cells become a confluent monolayer (Yeung et al., 2005). Similarly, the expansion of endothelial cell colonies is indifferent to changes in substrate stiffness (Trepat et al., 2009). The relative indifference of these properties to substrate rigidity has been attributed to the maintenance of cell–cell adhesions, which increases the effective stiffness cells sense beyond that of the underlying compliant substrate (Yeung et al., 2005;

Correspondence to Joan S. Brugge: Joan_Brugge@hms.harvard.edu; or Gaudenz Danuser: Gaudenz_Danuser@hms.harvard.edu

Abbreviations used in this paper: DN-Ecad, dominant-negative E-cadherin; fps, frames per second; MIIA, myosin-IIA; MIIB, myosin-IIB; PAA, polyacrylamide; PDMS, polydimethylsiloxane; pMLC, phosphorylated myosin-II regulatory light chain; shRNA, small hairpin RNA.

© 2012 Ng et al. This article is distributed under the terms of an Attribution–Noncommercial–Share Alike–No Mirror Sites license for the first six months after the publication date (see http://www.rupress.org/terms). After six months it is available under a Creative Commons License (Attribution–Noncommercial–Share Alike 3.0 Unported license, as described at http://creativecommons.org/licenses/by-nc-sa/3.0/).

The Rockefeller University Press $30.00
J. Cell Biol. Vol. 199 No. 3 545–563
www.jcb.org/cgi/doi/10.1083/jcb.201207148

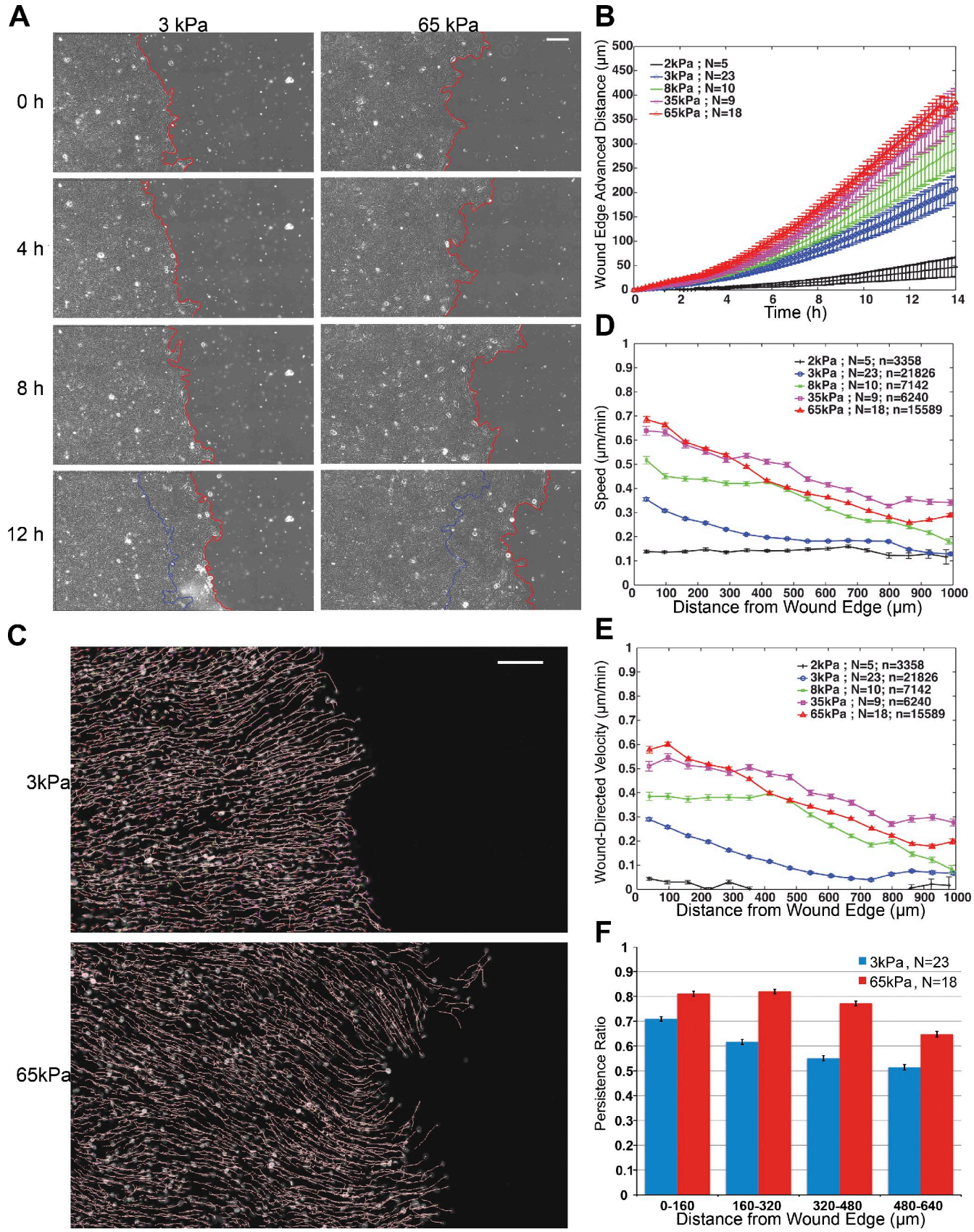

Figure 1. **Collective migration of MCF10A epithelial cell sheets on PAA gel substrates of various compliances.** (A) Progression of wound healing on soft (3 kPa) and stiff (65 kPa) substrates. Red lines trace the wound edge; blue line on 12-h images reflects the wound edge at 0 h after wounding. (B) The distance advanced by cell sheets over 14 h of wound healing on various substrate stiffnesses. (C) Tracks of cell movements overlaid with images of H2B-mCherry–labeled nuclei in cell sheets at 12 h after wounding on soft (3 kPa) and stiff (65 kPa) substrates. (D and E) Mean speed (D) and mean

Trepat et al., 2009). However, other studies concluded that substrate stiffness does affect collective migration. Increasing substrate stiffness was found to promote the scattering and migration of fibroblasts and epithelial cells from cell clusters in vitro (de Rooij et al., 2005; Guo et al., 2006; Saez et al., 2007) as well as the migration of neonatal rat heart tissue cells from tissue explants ex vivo (Guo et al., 2006). For confluent epithelial sheets, modulating the viscoelasticity of the substrate was also found to influence coordination in cell movement velocities (Murrell et al., 2011).

Our study sought to systematically investigate whether and how substrate stiffness affects epithelial sheet migration. We developed a wound-healing assay suitable for the study of collective migration on PAA gel substrates with a range of compliances and performed long-term fluorescent time-lapse imaging to monitor the movement of MCF10A epithelial cell sheets into the wound region. Using nuclei detection and tracking software, we characterized cell movements and cell–cell coordination in the sheet and analyzed effects of substrate stiffness, cell–cell adhesion, and myosin contractility. Our results indicate that cells at the wound edge sense substrate stiffness, and this information is relayed to cells further back in the sheet through mechanical cell–cell interactions, which depend on cadherin-mediated cell–cell adhesions and actomyosin contractility. We also show that the efficiency of this mechanical communication gradually decays over larger distances from the wound edge in a substrate stiffness-dependent fashion. Overall, our analysis of collective cell migration under various mechanical and molecular conditions offers new insights into how the mechanical microenvironment and cell–cell adhesions regulate sheet migration.

Results

We investigated how substrate stiffness affects collective migration of immortalized mammary epithelial cell (MCF10A) sheets using a wound-healing assay on compliant PAA gel substrates. To prevent damage to the substrates by wound scratching, we used a constraint removal method that involves placement of a physical barrier over a portion of the matrix substrate (Block et al., 2004; van Horssen et al., 2006; Poujade et al., 2007). Removal of the barrier opens up a "wound," into which the cells migrate (Fig. S1, A and B; and Video 1). By varying the cross-linking ratios of the PAA gel, we modulated the stiffness of the substrate in the range from 2 to 65 kPa.

Substrate stiffness affects the speed of epithelial cell sheet migration

We measured the sheet edge advancement over a time period of 14 h after barrier removal using automated tracing of the wound edge (Fig. 1 A). Irrespective of the substrate stiffness, the sheet edge accelerated within the first few hours, reaching a steady-state speed 8–10 h after wounding. The overall distance covered by the migrating sheet in 14 h increased with increasing substrate stiffness (Fig. 1 B and Video 1). This correlation was also observed with collagen-I coating (Fig. S1 C).

The contribution of cell proliferation to wound healing was minimal on both soft and stiff substrates, similar to previous observations on glass substrates (Poujade et al., 2007). Inhibition of cell division with mitomycin C (Wrobel et al., 2004) did not significantly decrease sheet edge advancement (Fig. S1, D and E). Rather, the advancement of the sheet was achieved by spreading and translocation of existing cells. This is further indicated by the decrease in cell density as the sheets advanced into the wound (Fig. S1 F) and the increase in mean cell area at the wound edge (Fig. S1 G). The increase in cell area was greater on stiffer substrates and was likely not accompanied by a change in cell volume because the mean cell height was lower on stiffer substrates (Fig. S1 H).

Substrate stiffness affects the migratory behaviors of single cells within a cell sheet

Next, we examined the migratory properties of individual cells within the sheet using a custom nuclei detection and tracking software (Fig. 1 C and Video 2; Jaqaman et al., 2008). The migration speed of individual cells within the cell sheet increased with increasing substrate stiffness (Fig. 1 D), consistent with faster wound closure on stiffer substrates. Interestingly, the epithelial sheet showed a broader range of rigidity sensing and response compared with sparsely seeded cells, which displayed high sensitivity of migration speed to substrate stiffness between 2 and 3 kPa but little sensitivity in the range of 8–65 kPa (Fig. S2 A).

We also found that the migration speed of individual cells decreased as a function of the cells' distance from the wound edge (Figs. 1 D and S2 B). The presence of this gradient is independent of substrate stiffness and has been observed in a previous study using glass substrates (Farooqui and Fenteany, 2005).

To assess the directionality of individual cell movements, we projected the velocities of cells undergoing collective migration onto the direction of wound closure (Figs. 1 E and S2 C). On the softer substrates (2 and 3 kPa), the mean projected cell migration velocity was lower compared with that on stiffer substrates (35 and 65 kPa) and dropped rapidly toward zero for cells further from the wound edge in the cell monolayer. In contrast, on the stiffer substrates, cells >500 µm from the wound edge contributed positive velocity in the direction of wound healing. These results indicated that cells migrate with greater directionality toward the wound and suggested that guidance cues extended further into the sheet on stiffer substrates.

wound-directed velocity (E) of individual cells within the collectively migrating cell sheet at 12 h after wounding, plotted as a function of cell distance from the wound edge. (F) Mean cell migration persistence for cells positioned at various distances from the wound edge after 5 h of migration starting at 8 h after wounding. *N* = number of experiments; *n* = total number of cells measured from *N* experiments. Error bars show 95% confidence interval of the mean (95% SEM); all nonoverlapping error bars are statistically significant with $P < 0.05$. Bars, 100 µm.

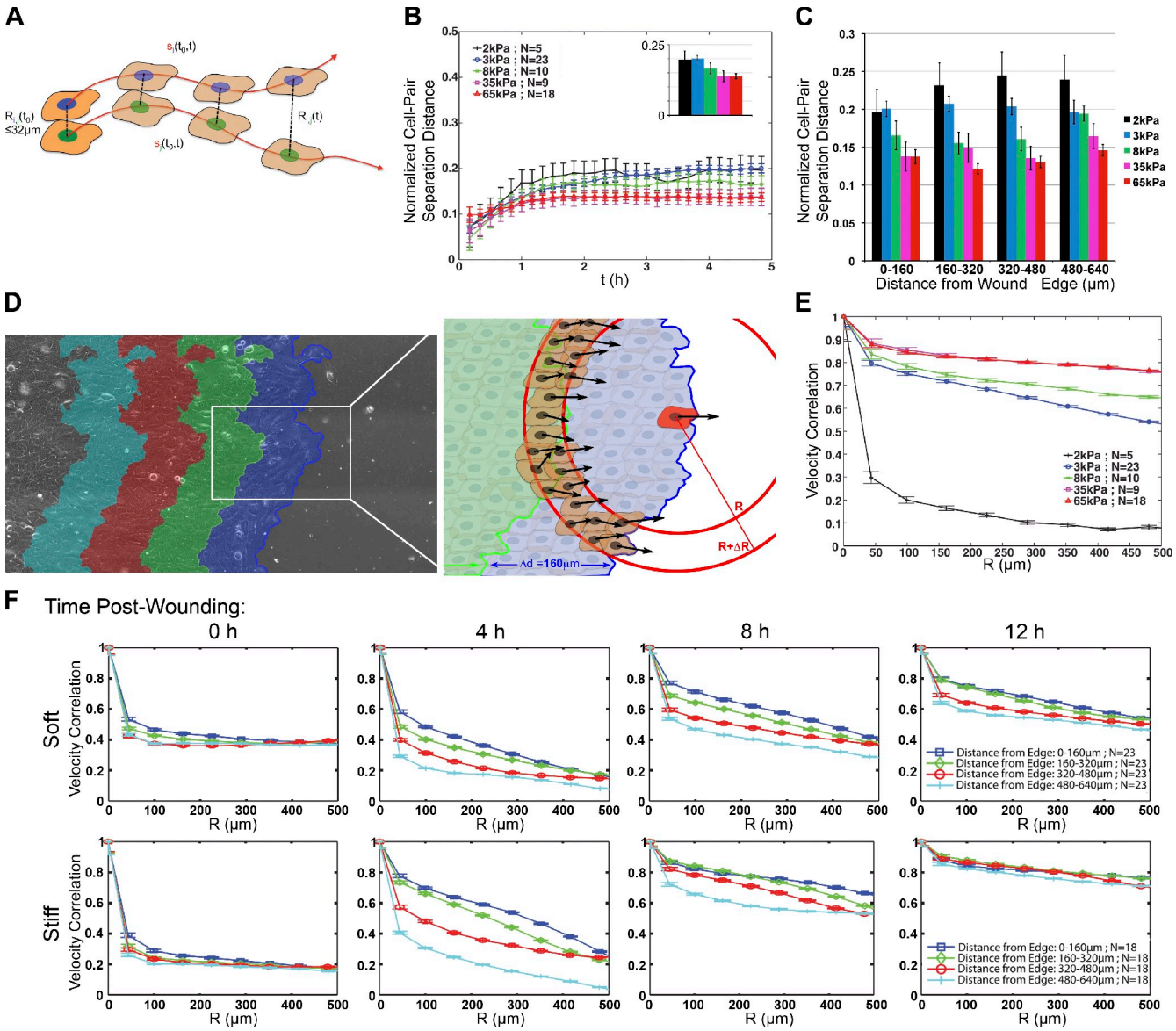

Figure 2. **Coordination of cell movements on soft and stiff substrates.** (A) Depiction of normalized cell pair separation distance measurement. Measurements were made starting 8 h after wounding (t_0). See Materials and methods for details. (B) Mean normalized cell pair separation distance over a time course (t) of 5 h for all neighboring cell pairs within 160 µm from the wound edge. (inset) Mean cell pair separation distance at the end of the 5-h observation window for different substrate stiffness. (C) Mean normalized cell pair separation distance as a function of cell position from the wound edge for different substrate stiffness. (D) Depiction of velocity correlation measurement. The migrating cell sheet was divided into bands of 160 µm starting from the wound edge. (inset) For each band, the velocities (arrows) of all cells were correlated with those of other cells falling in a ring of radius R and width ΔR and then averaged. See Materials and methods for details. (E) Velocity correlation 12 h after wounding for cells 160 µm from the wound edge for different substrate stiffness. (F) Velocity correlation as a function of cell–cell distance R, for cells in different distance bands from the wound edge and at different time points after wounding. N = number of experiments. Each plot displays means of 150–3,000 cell measurements pooled from N experiments. All nonoverlapping error bars (95% SEM) are statistically significant with $P < 0.05$.

We also examined the difference in migration persistence between cells on soft and stiff substrates. We measured the ratio of the net path length over the total path length for a period of 5 h starting at 8 h after wounding, the time point when the collective migration rate reached a constant value (Figs. 1 F and S2 D). On both soft and stiff substrates, cells closer to the wound edge migrated more persistently than cells further from the wound edge. However, cells across all distances from the wound edge migrated more persistently on stiffer than on softer substrates. In addition, on the stiff substrates, cells 0–160, 160–320, and 320–480 µm from the sheet edge all migrated with similarly high persistence. Together with the speed and directionality measurements, these data indicated that substrate stiffness modulates the migration of individual cells within the sheet, with increased stiffness correlating with increased cell migration speed, directional migration toward the wound, and persistence.

Increase in substrate stiffness increases coordinated motion during collective migration

The dependency of migration parameters on substrate stiffness suggested that the coordination of cell movements during

collective migration could be responsive to the mechanical microenvironment. To test this, we determined cell–cell coordination using two measures. First, we measured the change in relative distance between two neighboring cells over a 5-h time period (Fig. 2 A). To render the measurement invariant to differences in cell migration speed, we normalized the cell pair separation distance by the mean traveled distance of the two cells. Thus, an increase in the normalized cell pair separation distance would indicate greater cell dispersion or cell mixing. For all stiffness levels, the normalized cell pair separation distance measured between 8 and 13 h after wounding gradually increased before reaching a steady state. The steady-state cell pair separation distance was significantly higher on soft substrates (2 and 3 kPa) than on stiff substrates (35 and 65 kPa; Fig. 2 B), both for cells near the wound edge and cells located hundreds of micrometers behind the wound edge (Fig. 2 C).

Second, we measured the distance-dependent correlation in migration velocities between cells at specific time points (Fig. 2 D). Correlation values were calculated for cell–cell distances in the range of 0–500 µm and averaged in bands of 160 µm from the wound edge. This provided a measurement of the long-range motion coordination of cells as a function of cell position within the sheet. On both soft and stiff substrates, the velocity correlation decreased with increasing cell–cell distance. Importantly, velocity correlation between cells for all cell–cell distances is higher on stiffer substrates (Fig. 2 E), consistent with the normalized cell pair separation distance. Furthermore, on both soft and stiff substrates, the correlation increased as wound healing progressed over time, with cells near the wound edge being more correlated in their migration velocities than cells farther from the wound edge (Fig. 2 F, 4 h and 8 h). Establishment of high velocity correlation propagated into the cell sheet as time progressed. By 12 h after wounding, cells >480 µm from the sheet edge were correlated in their migration velocities similar to cells near the wound edge on stiff, but not on soft, substrates (Fig. 2 F). This is reminiscent of our observation that cells at a greater distance from the wound edge were able to migrate more directionally and persistently on stiff compared with soft substrates.

We noted that the migration of individual cells was significantly less coordinated when an epithelial sheet was unwounded or when cells were seeded sparsely (Fig. 3). Moreover, the extent of velocity correlation in unwounded sheets or sparsely seeded cells displayed little dependency, if any, on substrate stiffness (Fig. 3, B and C). Hence, only when cells respond to a directional cue, do they coordinate their movements in a substrate stiffness-dependent fashion.

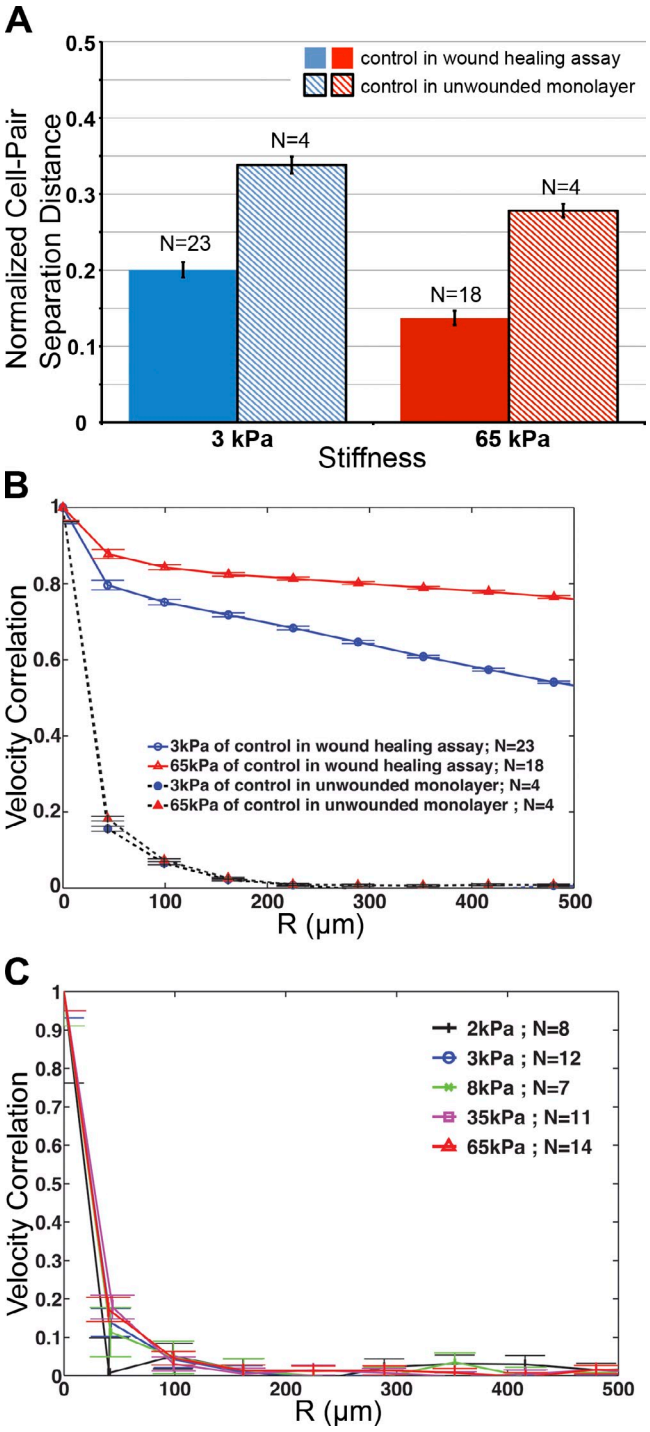

Figure 3. **Analysis of coordination of cell movements in unwounded monolayers and between sparse cells.** (A and B) Mean normalized cell pair separation distance (A) and mean velocity correlation (B) for confluent, unwounded MCF10A monolayers on soft (3 kPa) and stiff (65 kPa) substrates compared with those for cells within 160 µm of wound edge undergoing collective migration at 12 h after wounding. (C) Mean velocity correlation for sparsely seeded MCF10A cells on various substrate stiffness. *N* = number of experiments. All nonoverlapping error bars (95% SEM) are statistically significant with $P < 0.05$.

Substrate stiffness affects Golgi orientation and the direction of lamellipodial protrusions

Previous studies have shown that cell polarization is important for the directionality and persistence of cells migrating either as single cells (Ridley et al., 2003) or as leader cells during collective migration (Reffay et al., 2011). We therefore examined the direction of cell polarization by measuring the position of GFP-labeled Golgi with respect to the nuclei and the wound edge (Fig. 4 A). On stiff substrates, a majority of wound edge cells were polarized with the Golgi anterior to the nucleus early on in the wound-healing process (Fig. 4 B), consistent with other

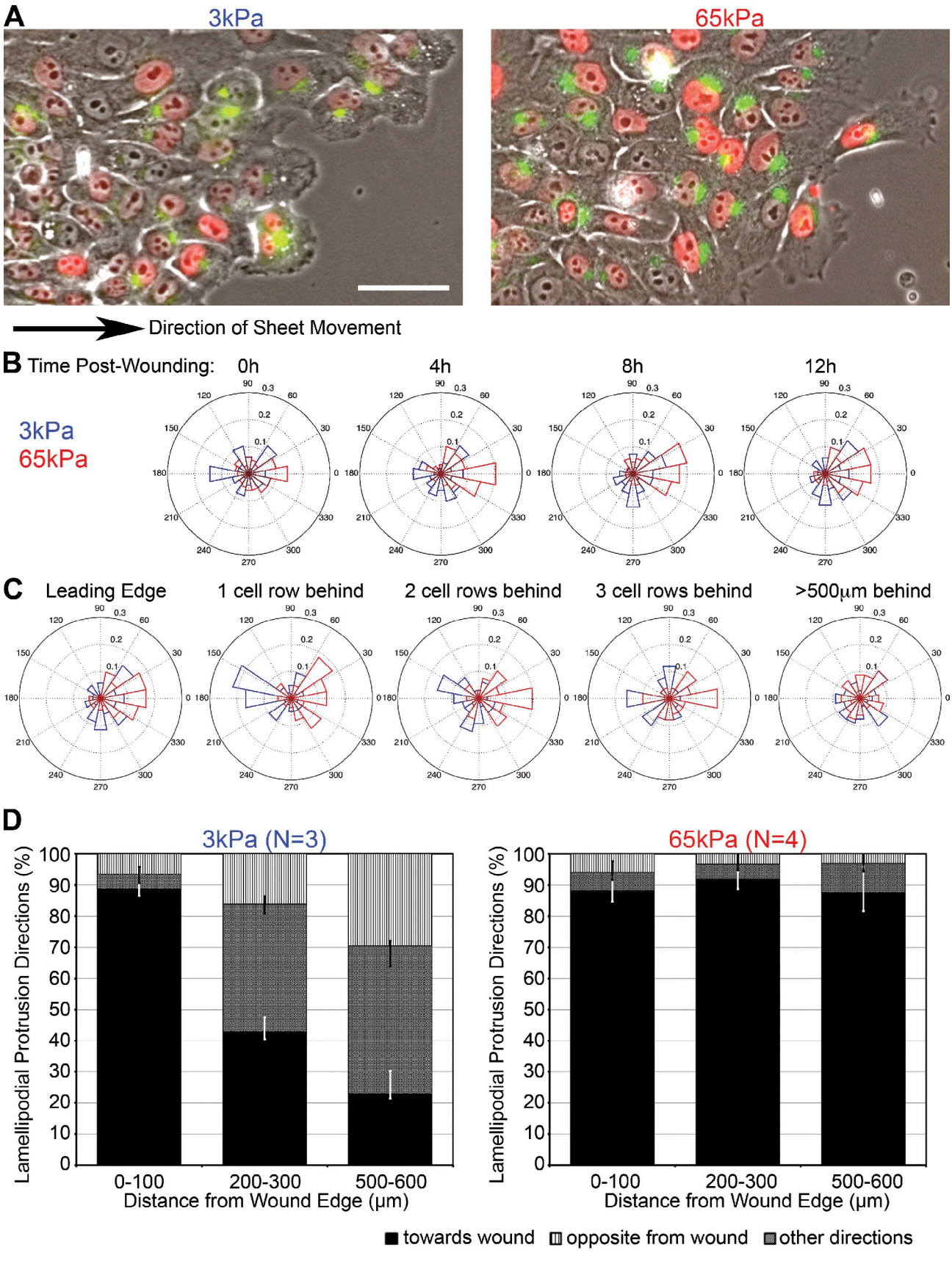

Figure 4. **Analysis of cell polarization orientations on stiff and soft substrates.** (A) MCF10As transfected with Golgi-GFP undergoing wound healing on soft (3 kPa) versus stiff (65 kPa) substrates. Bar, 50 µm. (B) The orientations of Golgi relative to the direction of wound healing, as measured from centroids of cell nuclei, were plotted in rose plots at various time points after wounding for cells at the wound edge. The direction of each bar in the rose plots indicates

studies (Desai et al., 2009; Dupin et al., 2009). In addition, cells several rows behind the wound edge were similarly polarized (Fig. 4 C). This correlated with the high coordination of cell movements on stiff substrates, which also extended from the wound edge into the cell sheet. On soft substrates, the polarization direction was less coordinated. Although the majority of wound edge cells were polarized at 12 h after wounding with the Golgi anterior to the nucleus, the Golgi orientation varied greatly just one cell layer behind the wound edge (Fig. 4 C). Because Golgi orientation is influenced by microenvironmental conditions (Pouthas et al., 2008; Desai et al., 2009; Doyle et al., 2009; Dupin et al., 2009), our results suggest that cell polarization on soft substrates is more influenced by local cell–cell, cell–matrix, and other morphological cues, whereas cells on stiff substrates are coupled globally.

Lamellipodial protrusions are also known to guide cell migration (Small et al., 2002; Ridley et al., 2003). During collective migration, cells at the wound edge and within the cell sheet all actively migrate, the latter with the aid of cryptic lamellipodial protrusions extended beneath adjacent cells (Farooqui and Fenteany, 2005). We therefore also evaluated the direction of lamellipodial or cryptic lamellipodial protrusions by confocal time-lapse microscopy of cells expressing GFP-paxillin. On stiff substrates, the protrusions extended mostly toward the direction of the wound closure, even for cells >500 µm from the wound edge. On soft substrates, the directions of the protrusions were more randomly distributed the farther the cells were located away from the wound edge (Fig. 4 D and Video 3). These results were consistent with our normalized cell pair separation distance and velocity correlation measurements. Together with the Golgi orientation measurements, they provided a cellular level explanation for the observation that cells migrate more coordinately on stiffer substrates.

Myosin-II contractility mediates the effects of substrate stiffness on collective migration properties

Analyses of single-cell migration revealed that cellular levels of myosin-II activity vary with substrate stiffness and that myosin-II–mediated contractility regulates cell spreading and migration (Schwarz et al., 2003; Peyton and Putnam, 2005; Gupton and Waterman-Storer, 2006). Therefore, we hypothesized that the sensitivity of collective migration properties toward substrate stiffness may be related to differential modulation of myosin-II activity. Indeed, cells on stiff substrates had higher myosin activity in MCF10A monolayers, as indicated by the higher level of serine19–phosphorylated myosin-II regulatory light chain (pMLC) detected by immunostaining (Fig. 5 A). pMLC staining was localized along actin fibers that aligned along the long axes of cells, and its level was higher in cells at the wound edge than in cells embedded >400 µm within the cell sheet on both soft and stiff substrates (Fig. 5 B). Furthermore, cellular myosin activity correlated with focal adhesion size, which was higher in collectively migrating cells on stiff substrates, particularly at the wound edge (Figs. 5 C and S3 A). These results are consistent with previous studies of single cells having higher myosin activity (Engler et al., 2006; Clark et al., 2007a; Kuo et al., 2011) and larger focal adhesions (Pelham and Wang, 1997; Engler et al., 2004; Prager-Khoutorsky et al., 2011) on stiffer substrates. These data suggested that the decrease in coordinated movement between cells on soft substrates may be caused by reduced myosin-II activity and that myosin-II activity may be important for relaying directional guidance cues from the wound edge into the sheet.

To examine this possibility, we reduced myosin-II activity in cell sheets on soft and stiff substrates either using blebbistatin treatment or by knockdown of nonmuscle myosin-II isoform A (MIIA) or myosin-II isoform B (MIIB; Fig. S3, B and C). Treatment with blebbistatin decreased cell migration speed on stiff substrates to values similar to those on soft substrates (Fig. 5 D). Interestingly, the treatment had almost no effect on cell speed on soft substrates, consistent with the overall lower level of myosin-II activity. Knockdown of the individual myosin-II isoforms also significantly decreased cell migration speed on stiff substrates, although to a lesser extent than blebbistatin treatment, most likely because of residual myosin-II activity by the myosin-II isoform not targeted (Fig. S3, D and E). Moreover, decreased myosin-II activity also increased cell pair separation distance and decreased velocity correlation during collective migration (Figs. 5, E and F; and S3, F–I; and Video 4). Together, our data show that myosin-II–mediated contractility contributes significantly to differences in cell migration speed, persistence, and cell–cell coordination on matrices of different compliances.

Regulation of cell–cell coordination by substrate stiffness depends on cadherin-mediated cell–cell adhesions

We next investigated how perturbations in cell–cell adhesion proteins affect cellular responses to variations in substrate stiffness. Cell–cell adhesion molecules have been shown to be important for collective migration in vitro (Macpherson et al., 2007; Simpson et al., 2008; Vitorino and Meyer, 2008) and in vivo (Niewiadomska et al., 1999) and are thought to be critical for coordinating cell movements (Arboleda-Estudillo et al., 2010; Murrell et al., 2011; Tambe et al., 2011). We chose to focus our investigation on cadherin-mediated cell–cell adhesions as those are particularly relevant for maintenance of epithelial cell sheets (Simpson et al., 2008). Although disruption of adherens junctions by siRNA-mediated knockdown of P-cadherin (siCDH3) increased the migration speed of cells near the wound edge, it had no significant effect on the advancement

the angular Golgi orientations, whereas the magnitude of each bar shows the fraction of cells with the indicated Golgi orientations. (C) Rose plots of Golgi orientations at 12 h after wounding for cells at various rows behind the wound edge cells. (D) The primary direction of lamellipodial protrusions in cells on soft (3 kPa) and stiff (65 kPa) substrates was quantified as in the direction of wound healing, opposite the direction of the wound, and toward other directions. Measurements were obtained for >30 cells at various distances from the wound edge from *N* experiments. Error bars show SEM.

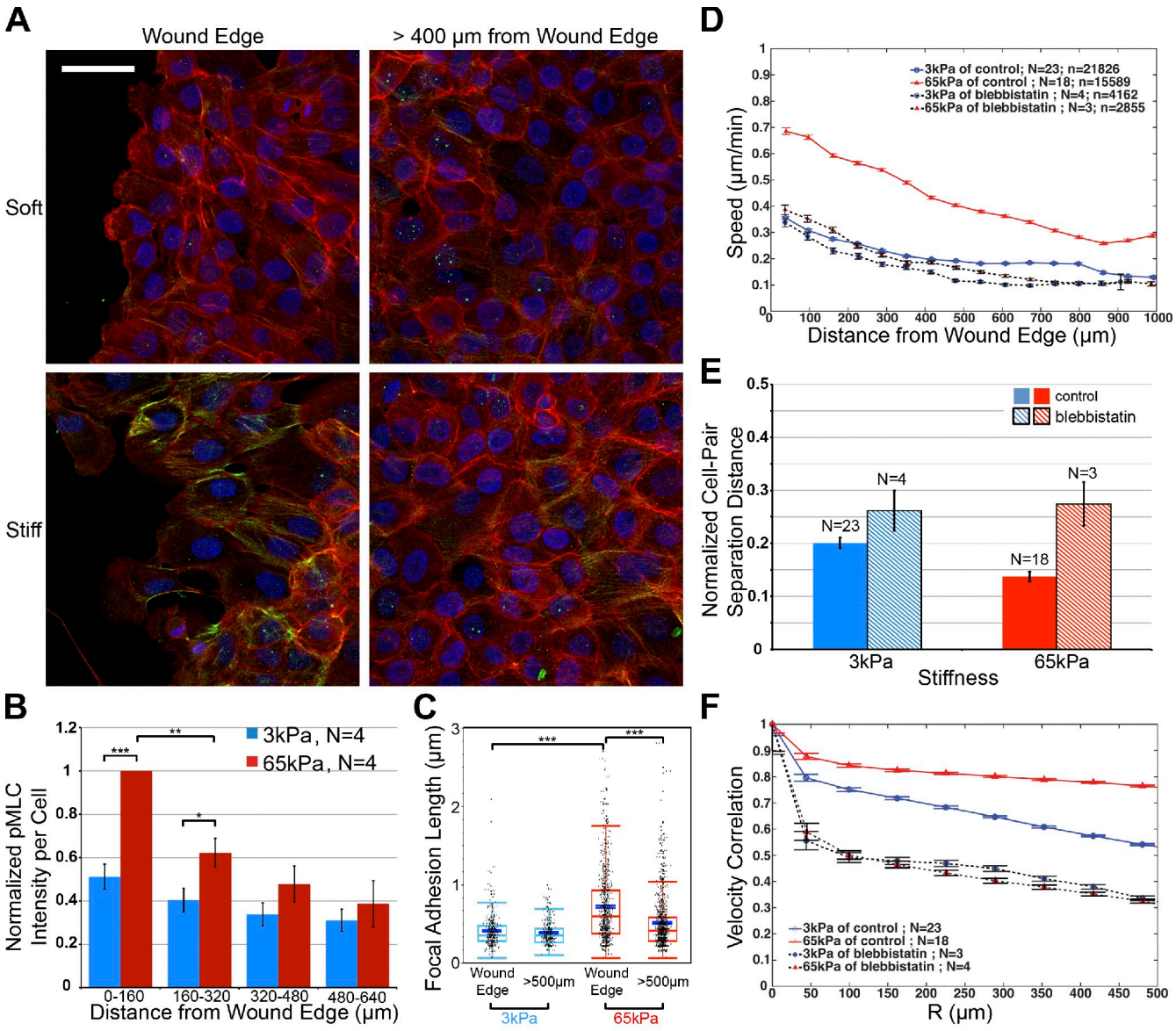

Figure 5. **The effects of myosin-II contractility on collective migration on soft and stiff substrates.** (A) Maximum intensity projection of z-stack images of collectively migrating cells on soft and stiff substrates immunostained with pMLC (green), phalloidin as actin marker (red), and DAPI as the nuclei marker (blue). Bar, 50 µm. (B) Spatial variation of pMLC fluorescent intensity normalized by cell numbers. Error bars show SEM. (C) Focal adhesion lengths on stiff and soft substrates. Blue bars within box plots indicate means and SEM; data points outside the whiskers are outliers. (D) Effects of 25 µM blebbistatin treatment on the mean speed of individual cells at 12 h after wounding on soft and stiff substrates. (E and F) Effects of 25 µM blebbistatin on mean normalized cell pair separation distance (E; after 5 h of observation starting 8 h after wounding, see Fig. 2) and velocity correlation at 12 h after wounding (F) on soft and stiff substrates for cells 160 µm from the wound edge. *N* = number of experiments; *n* = total number of cells measured from *N* experiments. *, $P < 0.05$; **, $P < 0.005$; ***, $P < 0.0005$. Nonoverlapping error bars in D–F (95% SEM) are statistically significant with $P < 0.05$.

of the wound edge compared with control cells on either stiff or soft substrates (Fig. 6, A and B). This is because the increase in migration speed was offset by reduced directional migration (Fig. 6 C), lowered migration persistence (Fig. 6 D), and disrupted coordinated motion (Fig. 6, E and F). Similar results were obtained when adherens junctions were disrupted by overexpression of a dominant-negative E-cadherin (DN-Ecad) variant (Onder et al., 2008) as well as siRNA-mediated knockdown of the cadherin-associated protein α-catenin (siCTNNA1; Fig. S4 and Video 5). Reduction of cell–cell adhesions also disrupted the coordination in Golgi orientation on both soft and stiff substrates (Fig. 6, G and H). Hence, cadherin-mediated cell–cell adhesions were indeed crucial for cell–cell coordination during collective migration, irrespective of substrate stiffness.

Interestingly, all methods used to reduce cadherin-mediated cell–cell adhesions not only lowered cell–cell coordination but also rendered the coordination in movements between these cells less responsive to differences in substrate stiffness. For example, the difference in the normalized cell pair separation distance between stiff and soft substrates became insignificant when adherens junctions were perturbed (Figs. 6 E and S4, H and N). Similarly, the difference in velocity correlation between cells on soft and stiff substrates

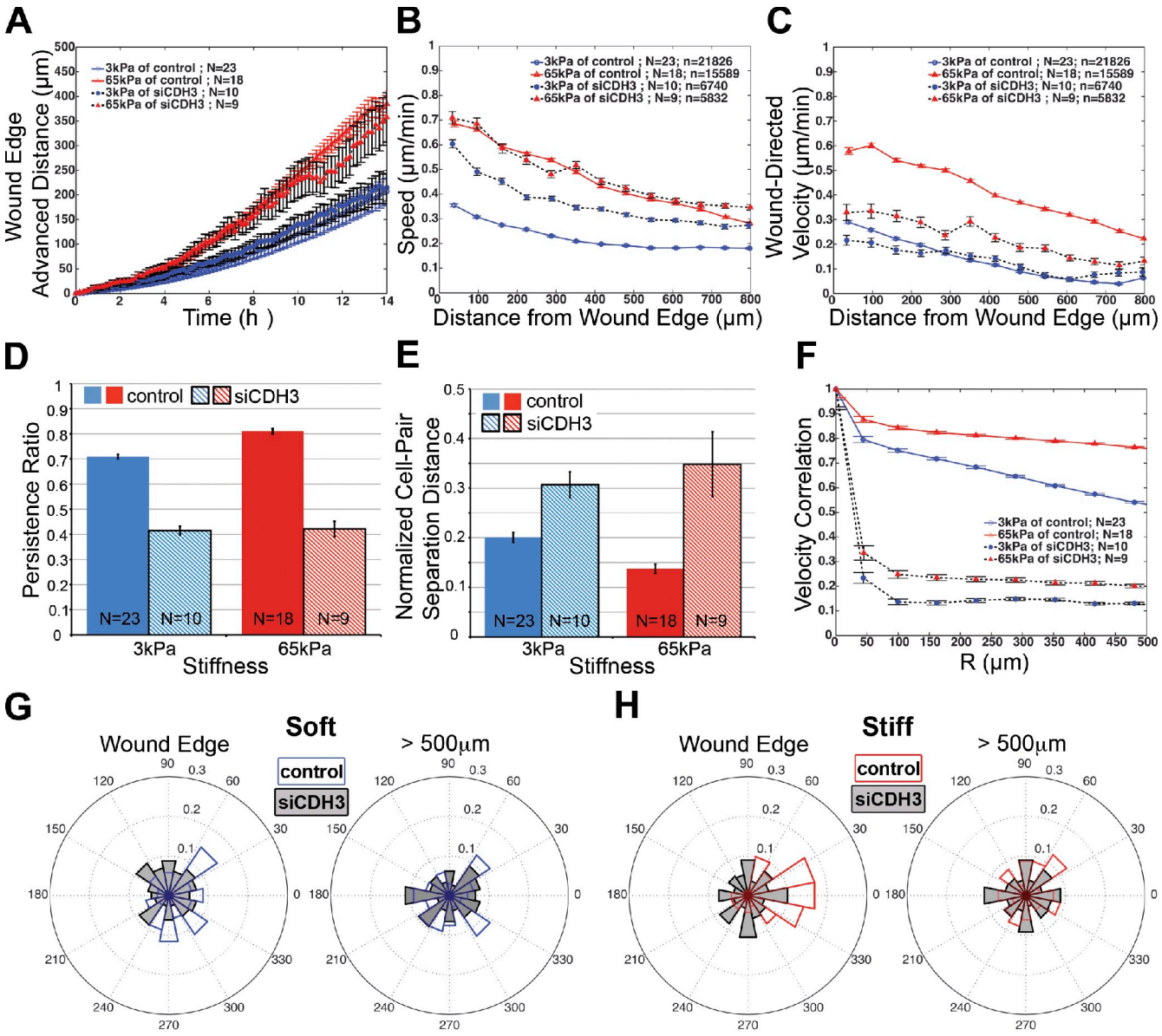

Figure 6. **The effects of P-cadherin knockdown (siCDH3) on migration properties during wound healing.** (A) Effects of siCDH3 treatment on mean distance advanced by the cell sheet. (B–F) Migration properties of siCDH3-treated cells undergoing wound healing on soft (3 kPa) and stiff (65 kPa) substrates, compared with control cells, plotted at same time points after wounding and distances from wound edge as in Figs. 1 and 5. (G and H) Golgi orientation at 12 h after wounding on soft (3 kPa) or stiff (65 kPa) substrates. *N* = number of experiments; *n* = total number of cells measured from *N* experiments. All nonoverlapping error bars (95% SEM) are statistically significant with $P < 0.05$.

was reduced when adherens junctions were targeted, especially for cells further apart (Figs. 6 F and S4, I and O). This showed that the influence of substrate stiffness on collective migration required the maintenance of cell–cell adhesions by adherens junctions.

To further investigate the role of cell–cell adhesions in rigidity sensing, we examined focal adhesions, actin structures, and pMLC levels in cells on soft and stiff substrates with or without disrupting cell–cell adhesions. Cells with siCDH3 or siCTNNA1 still had significantly larger focal adhesions on stiff substrates compared with on soft substrates. Nevertheless, the difference in focal adhesion sizes between wound edge cells and cells >400 μm from the wound edge on stiff substrates was reduced when adherens junctions were knocked down (Fig. S5, A and B). Perturbing cell–cell adhesions also disrupted the supracellular actomyosin fibers that aligned across multiple cells (Fig. 7 A). siCDH3 or siCTNNA1 also altered the pMLC level in cells. Although collectively migrating control cells showed higher pMLC levels at the wound edge compared with within the cell sheet (Fig. 5, A and B), disrupting cell–cell adhesions resulted in a diminished pMLC gradient for cells within 200 μm of the wound edge on stiff substrates, where the knockdown cells were mostly scattered (Fig. 7, A and B). Beyond 400 μm from the wound edge, where the knockdown cells were still in a monolayer, the pMLC immunofluorescence intensity was greatly decreased relative to the wound edge cells, and the decrease was more dramatic compared with that for control

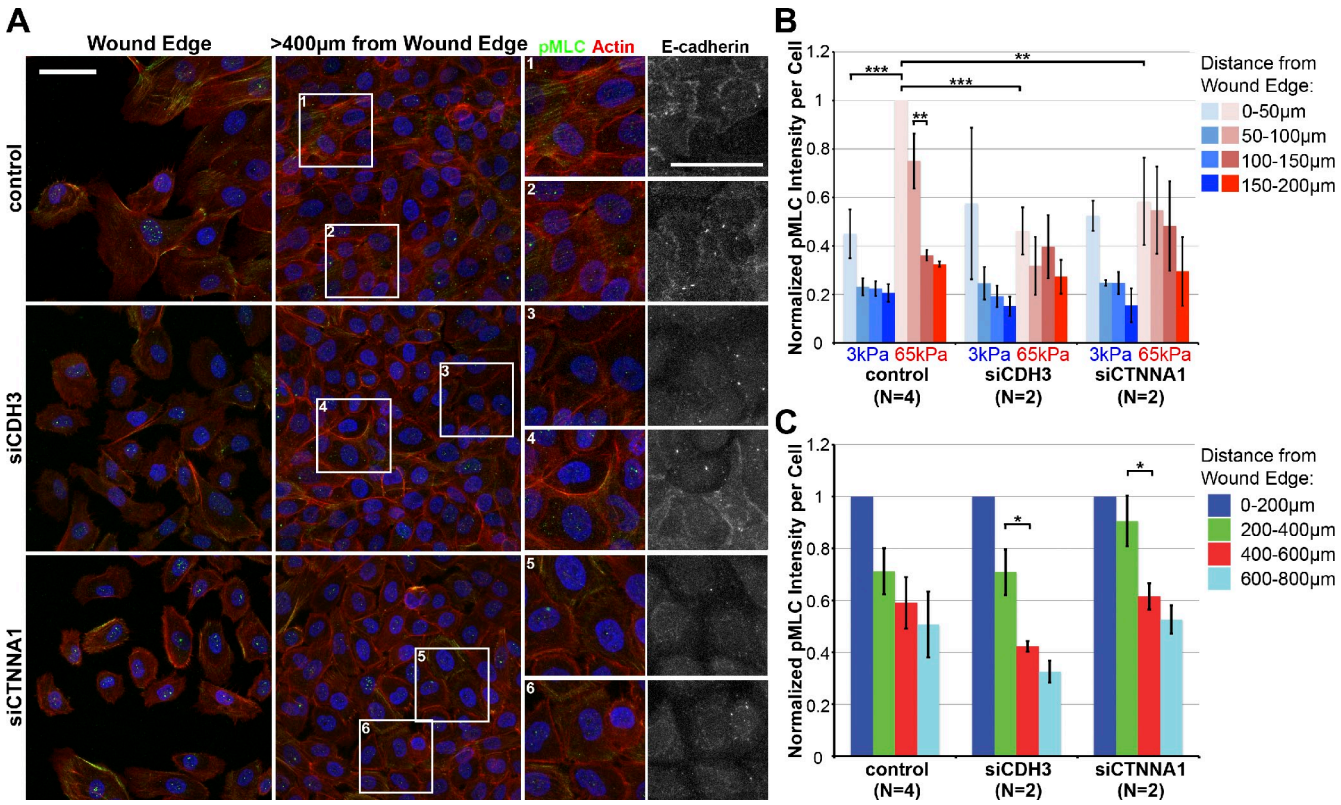

Figure 7. **The effects of siCDH3 and siCTNNA1 on actin organization and pMLC level in cells during wound healing.** (A) Maximum projections of confocal immunofluorescence images of pMLC (green) costained with phalloidin (red) and DAPI (blue) in control and knockdown cells at the wound edge and within the migrating cell monolayer. Insets are numbered and magnified at the right with corresponding maximum projection E-cadherin immunofluorescence images. Bars, 50 µm. (B) Quantification of pMLC fluorescence intensity per cell, normalized to that of the control wound edge cells on stiff substrates. (C) pMLC fluorescence intensity per cell on stiff (65 kPa) substrates, normalized to that of wound edge cells for each condition. Error bars show SEM. *N* = number of independent experiments. *, $P < 0.05$; **, $P < 0.005$; ***, $P < 0.0005$.

cells (Fig. 7 C). Hence, cells with reduced cell–cell adhesion seem unable to activate myosin-II–mediated contractility at large distances from the wound edge.

Low contractility attenuates the effects of disrupting cell–cell adhesions on coordinated migration

We noted that the reduction of cell–cell adhesions disrupted coordinated migration to a lesser extent on soft substrates, suggesting that low contractility attenuates the loss of coordination induced by the weakening of cell–cell adhesions (Fig. 6, E and F). In support of this possibility, cells in which both MIIA and α-catenin were down-regulated displayed better coordination and increased velocity correlation compared with cells in which α-catenin alone was down-regulated (Figs. 8, A and B; and S5 C). To further address the relationship between myosin contractility and cell–cell adhesion, we compared the effects of increasing concentrations of blebbistatin on control and P-cadherin down-regulated cells. Treatment of control cells with increasing concentrations of blebbistatin decreased cell–cell coordination. However, in cells treated with siCDH3 (which displayed weak cell–cell coordination), low concentrations (5 and 10 µM) of blebbistatin partially rescued the weak coordination (Figs. 8 C and S5, D and E; and Video 6). This suggests that cell contractility may promote or disrupt coordinated movement depending on the strength of cell–cell adhesions.

Discussion

Collective migration is mechanosensitive

The data collected in this study demonstrated significant differences in the speed, persistence, directionality, and coordination of individual cells during collective migration on soft versus stiff substrates. Strikingly, the coordination of cell movements extended deeper into the cell sheet from the wound edge on stiffer substrates. Similar to single migrating cells, mechanosensing and response of collectively migrating cells involve changes in myosin-II contractility levels (Figs. 5 and S3; Engler et al., 2006; Clark et al., 2007a; Kuo et al., 2011). However, the response to substrate stiffness was different between collective and single-cell migration (Figs. S1 and 3), suggesting distinct mechanisms for mechanosensing. We find that the presence of a directional cue, the maintenance of cell–cell adhesions, and the activity of myosin-II contractility are essential factors in collective rigidity sensing and response.

Wound edge cells promote the coordination and mechanoresponse of the migrating sheet

The presence of a common directional cue, in our case an open wound region, is required for a differential collective response of the cell sheet to varying substrate stiffness. Sparsely seeded cells migrating in the absence of a chemotactic or durotactic

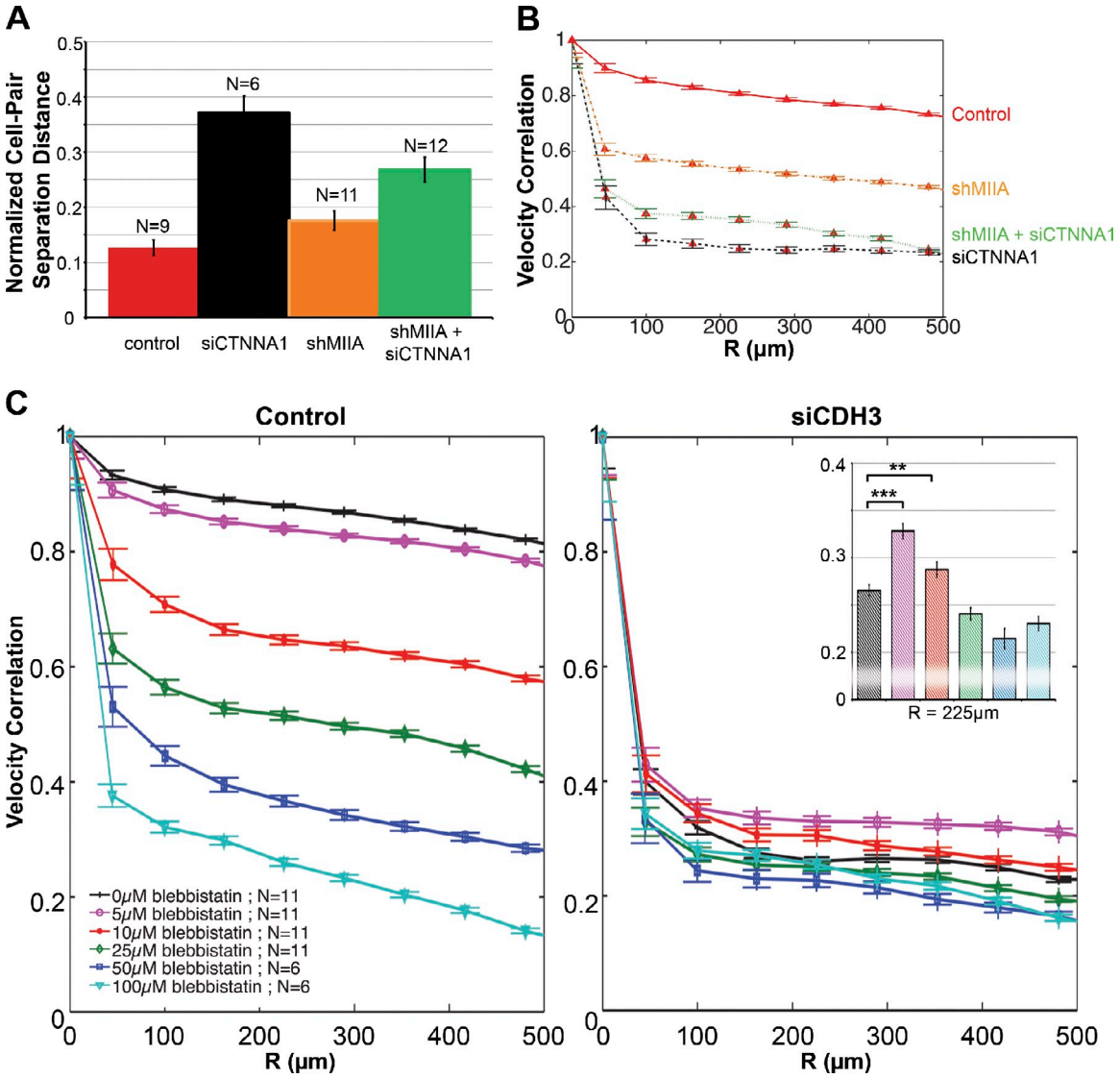

Figure 8. **Effects of lowering myosin contractility in cells with reduced cell–cell adhesions.** (A and B) Normalized cell pair separation distance (A) and velocity correlation (B) for control cells, cells treated with siCTNNA1, MIIA knocked down cells, and MIIA knocked down cells treated with siCTNNA1 on stiff (65 kPa) substrates. (C) Velocity correlation for control and siCDH3-treated cells on glass after blebbistatin treatment. Inset shows velocity correlation at R = 225 μm for siCDH3 cells. *N* = number of experiments. All nonoverlapping error bars (95% SEM) are statistically significant with $P < 0.05$. For the inset in C, statistical significance was specifically calculated for 0, 5, and 10 μM blebbistatin treatments to highlight the partial rescue in velocity correlation with low dose blebbistatin treatment. **, $P < 0.005$; ***, $P < 0.0001$.

gradient, or cells in a confluent but unwounded monolayer, displayed little to no correlation in migration velocities on either soft or stiff substrates (Fig. 3). This is consistent with a recent study showing that on elastic substrates, epithelial cells in an intact, confluent sheet exhibited only short-ranged cell–cell velocity correlation (Murrell et al., 2011). It may also explain why we detected significant differences in the behavior of cells on different substrate stiffness, whereas a previous study measuring unwounded, confluent cells did not (Yeung et al., 2005).

Both our study and previous studies showed that the directional cue is transmitted to cells embedded within the cell sheet by cells at or near the wound edge (Farooqui and Fenteany, 2005; Vitorino and Meyer, 2008; Trepat et al., 2009; Vitorino et al., 2011). For example, cells closer to the wound edge had greater wound-directed velocity (Fig. 1 E), lower normalized cell pair separation distance (Fig. 2, B and C), higher velocity coordination (Fig. 2, E and F), and greater percentages of wound-oriented cell polarization (Fig. 4, A–C) and lamellipodial protrusion (Fig. 4 D) on both soft and stiff substrates. The strongest evidence for a front-to-back guidance is the time evolution of velocity correlation after wounding (Fig. 2 F). Cells closer to the wound edge became coordinated first followed by a wave of coordination propagating into the sheet, irrespective of substrate stiffness (Fig. 2 F and Video 2).

The directional guidance provided by wound edge cells enhanced the response of the migrating cell sheet to substrate compliance. Velocity correlations for cells in sparsely seeded cultures or unwounded monolayers were not only low but also invariant to changes in substrate stiffness (Fig. 3). Furthermore, the wound edge cells displayed the greatest difference in migration

speed (Fig. 1 D), persistence (Fig. 1 F), spreading area (Fig. S1 G), focal adhesion size (Fig. 5 C), and myosin contractility (Fig. 5 B) on soft and stiff substrates compared with cells embedded within the migrating cell sheet. Thus, wound edge cells are more responsive to substrate stiffness than cells embedded within the cell sheet.

Collective rigidity sensing and response is dependent on cadherin-mediated transmission of the guidance cue during wound healing

Disruption of cell–cell adhesions by overexpressing DN-Ecad or by knocking down P-cadherin or α-catenin all consistently reduced the difference in migration properties, especially in cell–cell coordination, between cells on soft and stiff substrates (Figs. 6 and S4). Disrupting cell–cell adhesions also reduced the activation of myosin-mediated contractility even when the cells were on stiff substrates (Fig. 7). Cells embedded within the monolayer also displayed larger focal adhesions, similar to those of cells at the wound edge, when cell–cell adhesions were knocked down (Fig. S5, A and B). Hence, cell–cell adhesion influences cell–matrix mechanotransduction, which may be related to its role in relaying directional guidance cues from the wound edge into the sheet.

Previous experiments (Vitorino and Meyer, 2008; Tambe et al., 2011) and computational models (Lee and Wolgemuth, 2011; Vitorino et al., 2011) have demonstrated the importance of cell–cell junctions in transmitting guidance cues and promoting coordination during collective migration. Consistent with this, we found that disrupting cell–cell adhesions significantly reduced cell migration directionality, persistence, and coordination during wound healing (Figs. 6 and S4). In addition, we showed that the adherens junctions in cells during collective migration were connected with the actomyosin network (Figs. 5 and 7). This suggested that contractile forces were transmitted between cells through cell–cell adhesions. Down-regulating cell–cell adhesions perturbed the supracellular actin fiber organization and the gradient in pMLC activation that propagated from the wound edge cells on stiff substrates (Fig. 7). Together, these data suggest that cell–cell adhesions transmit mechanical cues sensed by the wound edge cells during collective migration.

Substrate stiffness regulation of coordinated movement depends on the balance between myosin-II contractility and cell–cell adhesion strength

Finally, our results demonstrated the importance of balance between cell–cell adhesions and myosin contractility for mechanosensation in collective migration. In the presence of cell–cell adhesions, myosin-II contractility contributed positively to coordinated movement. Lowering contractility by blebbistatin treatment or myosin knockdown reduced coordinated movement (Figs. 5 and S3), consistent with previous studies of increased cellular protrusive activities and decreased wound-directed migration with reduced myosin contractility (Farooqui and Fenteany, 2005; Kolega, 2006). Our data also supported the importance of myosin-II activity in regulating collective migration in vivo, such as during *D. discoideum* slug formation (Knecht and Shelden, 1995) and *Drosophila* border cell migration (Edwards and Kiehart, 1996).

On the other hand, we found that for cells with weakened cell–cell adhesions, a reduction in myosin-II activity by MIIA knockdown or by low doses of blebbistatin treatment could partially rescue the loss of cell–cell coordination (Figs. 8 and S5, D and E). Consistent with this, down-regulation of cell–cell adhesions disrupted coordinated movement less severely on soft substrates (Fig. 6), where myosin-II activity is already attenuated. These results suggest that high contractility impairs coordination of cells with weakened intercellular adhesion. Most interestingly, the partial rescue of coordinated movement in cells with knockdown of cell–cell adhesions was not detected at higher concentrations of blebbistatin treatment, indicating that sheet movement is more coordinated when cell contractility and the strength of cell–cell adhesions are balanced appropriately. The delicacy of this balance for coordinated migration is further indicated by the finding that increasing contractility at cell–cell adhesions could lead to a loss of cell–cell cohesion and disrupt collective migration (Hidalgo-Carcedo et al., 2011).

Model of mechanical regulation of collective migration

Collectively, our results support the model shown in Fig. 9 for the collective response of an epithelial sheet to substrate stiffness. Cells at the wound edge receive a directional cue, which causes them to polarize. Polarization involves the extension of protrusions, orientation of the Golgi anterior to the nucleus, and alignment of actin fibers, all in the direction of wound healing. Polarization is influenced by cellular actomyosin contractility and cell–cell adhesions, which physically link the cells within the cell sheet. Through these linkages, polarized contractile forces are transmitted to the submarginal cells. The submarginal cells respond to the directional forces by also polarizing and activating its myosin contractility. This process propagates into the cell sheet during collective migration, allowing for the rearward transmission of the directional cue. Substrate stiffness regulates this process by modulating cellular contractility through cell–matrix mechanotransduction, especially at the wound edge. Based on this model, down-regulation of myosin-II activation by softer substrate, blebbistatin treatment, or MIIA knockdown all reduces the contractile forces transmitted between cells and therefore the transmission of the directional cue. Similarly, down-regulation of cell–cell adhesions disrupts the force-mediated transmission of directional cues.

Although we cannot rule out contributions from soluble factors and signaling molecules (Fenteany et al., 2000; Matsubayashi et al., 2004; Yin et al., 2007; Block and Klarlund, 2008), a mechanical transmission of the directional cue is not only supported by our data but implicit in the results of other studies. Cells have been shown to exert shear stresses on each other during collective migration (Trepat et al., 2009; Tambe et al., 2011), and cadherin-mediated cell–cell adhesions do transmit forces (Liu et al., 2010; Maruthamuthu et al., 2011). Furthermore, these forces are able to direct cell protrusions (Weber et al., 2012).

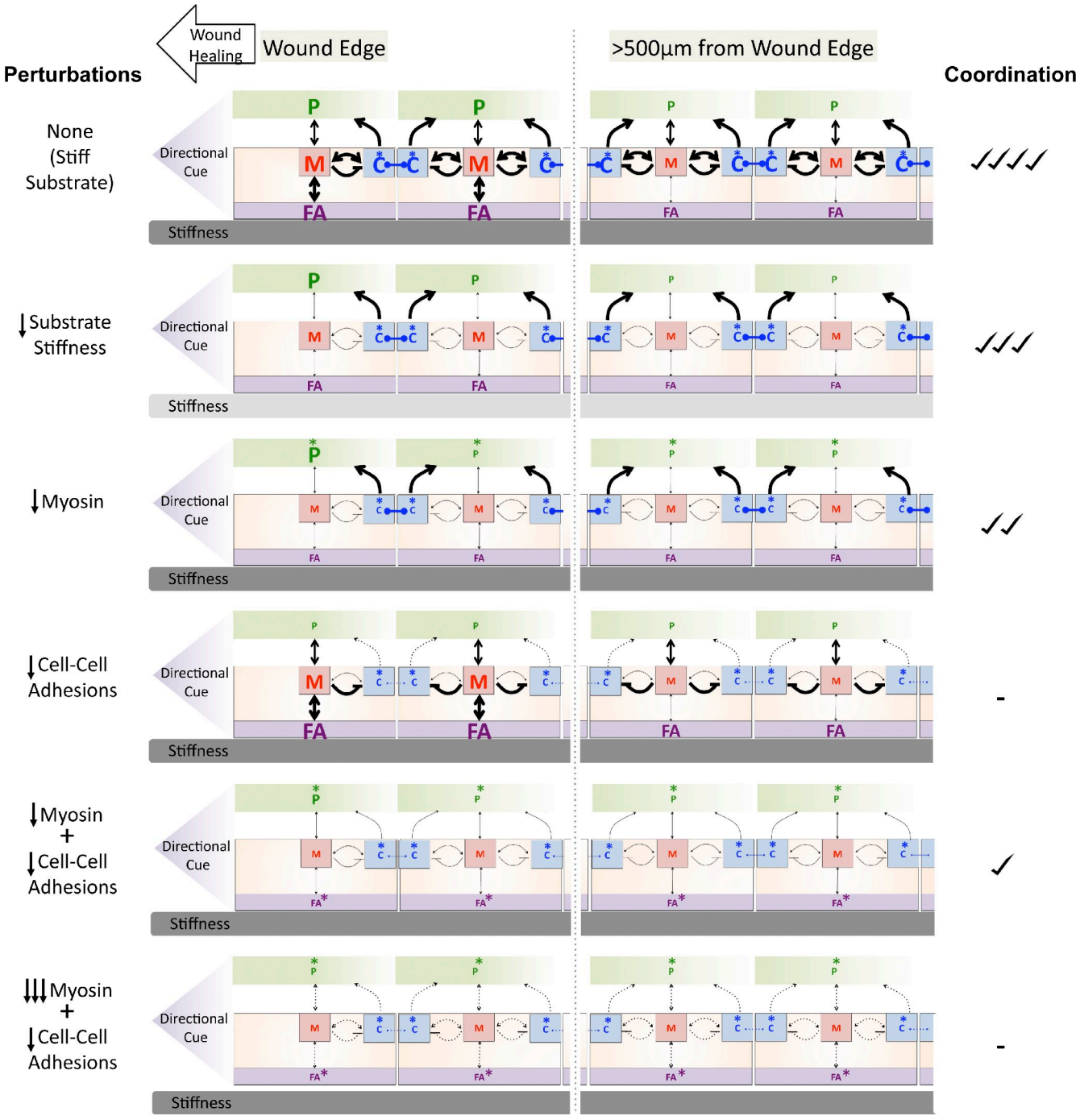

Figure 9. **Side view model of mechanoresponsive collective migration of MCF10A cells.** To achieve coordination in cell movements, cells at the wound edge respond to directional cue by front-rear polarization (P) in the direction of wound healing. The establishment and maintenance of cell polarity require actomyosin contractility (M), and they are influenced by cell–cell adhesions (C). Actomyosin contractility is governed by focal adhesions (FA) and cell–cell adhesion signaling. At the same time, actomyosin contractility promotes the formation and maturation of both focal adhesions and cell–cell adhesions (double-headed arrows). Actomyosin contractility can also be a negative regulator of cell–cell adhesions (flat-end arrow). The feedback coupling between actomyosin contractility and focal adhesions is stronger on stiff substrates and at the wound edge compared with >500 µm into the sheet, whereas within the sheet, the coupling between actomyosin contractility and cell–cell adhesions is stronger than between actomyosin contractility and focal adhesions. Forces generated by actomyosin contractility are transmitted to neighboring cells across cell–cell adhesions (blue dots connected by a line), where they activate actomyosin contractility and promote front-rear polarization in the follower cells. Propagation of front-rear polarization beyond the wound edge into the monolayer leads to cell–cell coordination. Various perturbations studied in this work affect focal adhesions, actomyosin contractility, and cell–cell adhesions, which in turn affect force transmission and front-rear polarization, leading to different levels of motion coordination. The sizes of the letters reflect relative magnitudes, and letters with asterisks indicate a parameter that is inferred and not directly measured in this study. All arrows are inferred, and the widths of the arrows reflect the relative strengths of interactions compared across the scenarios.

Our model offers insights into the cross talk between cell–matrix adhesions, actomyosin contractility, and cell–cell adhesions during sheet migration. We speculate that the coupling between cell–matrix adhesions and the actomyosin network is stronger closer to the sheet edge, whereas within the cell sheet, cell contractility is more influenced by cell–cell adhesions. This explains why substrate stiffness affects wound edge cells more than cells within the epithelial sheet. This also provides an explanation for the inability of cells with weakened cell–cell adhesions to up-regulate myosin contractility deep within the sheet, despite having larger focal adhesions than control cells (Fig. S5, A and B). Our model further includes a negative regulation of cell–cell adhesions by high actomyosin contractility. When cell–cell adhesions are weakened, the negative regulation leads to complete disruption of the connection and thus loss of motion coordination. Reduction, but not complete abrogation, of myosin contractility dampens the negative regulation and partially rescues the coordination between cells with weakened cell–cell adhesions.

The insight that substrate stiffness can influence properties of collective migration opens the door to new hypotheses in studies of morphogenesis, wound healing, and cancer cell invasion. For example, changes in substrate stiffness resulting from differential deposition or organization of ECM proteins during organotypic branching morphogenesis (Sakai et al., 2003; Larsen et al., 2006; Williams et al., 2008; Mori et al., 2009; Muschler and Streuli, 2010) may serve to locally promote coordination in the collective migration process. Changing stiffness associated with matrix deposition during wound healing may also promote coordinated collective migration for reepithelialization (Martin, 1997; Li et al., 2007), and modulation of matrix stiffness could be exploited in the design of engineered scaffolds to accelerate wound healing (Clark et al., 2007b; Ghosh and Ingber, 2007; Macri and Clark, 2009). Finally, increased substrate stiffness leading to greater collective migration speed and coordinated movement could be an important factor in the enhanced tumor invasion associated with matrix stiffening (Wozniak et al., 2003; Paszek et al., 2005; Alcaraz et al., 2008; Levental et al., 2009).

Methods and materials

Cell culture

MCF10A cells expressing H2B-mCherry as a nuclear marker were generated by infection with the pBabe-H2B-mCherry retroviral vector and selected with 300 µg/ml hygromycin. MCF10A cells were maintained in DME/F12 media supplemented with 5% horse serum, 20 ng/ml EGF, 0.5 mg/ml hydrocortisone, 100 ng/ml cholera toxin, 10 µg/ml insulin, and penicillin/streptomycin (Debnath et al., 2003).

Constraint-removal wound-healing assay on PAA gel substrates

PAA gel substrates were prepared on 12-well glass-bottomed dishes (MatTek Corporation) similar to methods previously described (Pelham and Wang, 1998). The glass surfaces were first modified by subsequent incubations with 0.1 N NaOH, 3-aminopropyltrimethoxysilane (Sigma-Aldrich), and 0.5% glutaraldehyde (Sigma-Aldrich). After washing and air drying, a drop of acrylamide/bis-acrylamide solution containing ammonium persulfate (Bio-Rad Laboratories, Inc.) and tetramethylethylenediamine (Sigma-Aldrich) was pipetted onto the modified glass surfaces. A coverslip was immediately placed over the droplets to ensure the formation of a flat gel surface after the solution polymerized. The bifunctional cross-linker sulfosuccinimidyl hexonoate (Thermo Fisher Scientific) was used to couple ECM proteins to the PAA gel substrates. Unless otherwise indicated, 10 µg/ml fibronectin (Sigma-Aldrich) was used as the ECM protein to functionalize the PAA gel substrates for cell seeding.

Generation of PAA gel substrates of various stiffnesses was performed by modulating the ratios of acrylamide to bis-acrylamide in solution. The ratios of acrylamide/bis-acrylamide used included 5:0.03%, 4:0.15%, 5:0.3%, 10:0.2%, and 10:0.3%, yielding stiffness of 2.05 ± 0.95, 3.05 ± 0.68, 8.33 ± 3.38, 33.90 ± 16.50, and 69.90 ± 21.76 kPa (∼2, 3, 8, 35, and 65 kPa), respectively. The elastic moduli were measured with the magnetic bearing rheometer (AR-G2; TA Instruments) and were generally consistent with literature values (Williams et al., 2008; Tse and Engler, 2010).

To conduct wound-healing assays on the PAA gel substrates, blocks of ∼5 mm wide × 13 mm long × 10 mm high were constructed using polydimethylsiloxane (PDMS) and blocked with 1% BSA in PBS for 1 h to protect against cell and matrix adhesions. A single PDMS block was placed atop the PAA gel substrate in each well. These PDMS blocks acted as a barrier to prevent cell adhesion to the PAA gel surfaces beneath the blocks. 3×10^5 MCF10A cells were then seeded in each well overnight. Immediately before imaging, the PDMS blocks were removed, allowing cell migration into the newly revealed cell-free, or "wound," region.

To verify that the PDMS block removal did not perturb the fibronectin coating, PAA gels were coated with 10 µg/ml rhodamine-labeled fibronectin (Cytoskeleton) in a set of control experiments. After block removal, multiple wide-field epifluorescence images were captured at both the wound regions and the nonwounded regions on all five substrate stiffnesses, and the fluorescence intensity of the rhodamine-fibronectin was measured using ImageJ (National Institutes of Health). Two independent experiments were performed.

Fluorescent time-lapse imaging of cell migration

Fluorescent time-lapse images of cell migration on PAA gel substrates were collected on an inverted motorized microscope (Ti-E; Nikon) equipped with a 20× Plan Apochromat 0.75 NA objective lens, a linear-encoded motorized stage (Nikon), a halogen trans-illuminator with a 0.52 NA long working distance condenser (Nikon), fast (<100-ms switching time) excitation and emission filter wheel with filters (excitation 480/40 nm and emission 525/50 nm for GFP; excitation 575/50 nm and emission 640/50 nm for mCherry; Chroma Technology Corp.), fast transmitted and epifluorescence light path shutters (SmartShutter; Sutter Instrument), a cooled charge-coupled device camera (ORCA-AG; Hamamatsu Photonics), a custom-built microscope incubation chamber maintained at 37°C and 5% CO_2, and an integrated Perfect Focus System (Nikon) for continuous maintenance of focus. Images were acquired every 10 min at multiple stage positions with 2 × 2 binning and using the large image setting in NIS-Elements AR software v3 (Nikon), such that the final images at each position were stitched from ∼4 × 3 or 3 × 3 fields of view. Phase and epifluorescence images capturing H2B-mCherry signals were acquired at every time point.

Image analyses and statistics

Unless otherwise noted, analyses of cell migration, including automatic wound edge tracing, nuclei detection and tracking, and calculations of spatial classification and cell migration parameters, were performed with custom-written MATLAB programs (MathWorks). For plots of speed, wound-directed velocity, persistence, normalized cell pair separation distance, and velocity correlation, means were calculated by binning the measurements from the fraction of cells located within indicated distance bands from the wound edge (see Spatial classification section for details). Measurements were pooled from *N* experiments. All error bars in plots of wound-edge advancement, speed, wound-directed velocity, persistence, normalized cell pair separation distance, and velocity correlation indicate errors of the mean at 95% confidence level. Nonoverlapping error bars in these plots therefore indicate statistical significance with $P < 0.05$.

Standard box plots were created using JMP 9 (SAS Institute, Inc.), with the bottom and top of the box extending from the first quartile to the third quartile (interquartile range), the red horizontal line within each box indicating the sample median, and the whiskers extending to the outermost data points that fall within 1.5× interquartile range below the first and above the third quartiles. If the data values did not reach the computed range, the whiskers were determined by the maximum and minimum data point values. Data points outside the whiskers indicate outliers. Blue lines inside the box plots indicate means ± SEM.

Automatic wound edge tracing and wound edge advancement distance measurement

The leading edges of the cell sheets during wound healing were enhanced from phase images by applying a steerable filter of first order (which corresponds to a canny edge detector) with standard deviation of two pixels. The implementation followed (Jacob and Unser, 2004). After filtering, a closing was applied to the image with a disc of five pixels in radius (r) as a structuring element. The images were then converted into a black and white mask by unimodal thresholding the intensity histogram of the image (Rosin, 2001). The largest nonzero connected component in the black and white mask corresponds to the cell sheet. Single cells that broke away from the sheet edge also generate a nonzero connected component. These isolated cells were, however, not considered as part of the migrating sheet. Potential holes within the sheet mask were closed, thus separating the image into two domains, one corresponding to the cell sheet and one to the open wound. To remove rough features along the sheet edge, the black and white mask was smoothed by image opening with a disk of 2× r as a structuring element. In the last step, the sheet edge was extracted as pixelated curve (Fig. 1, red lines; and Videos 1, 4, 5, and 6) from the black and white mask. The analysis stopped when the sheet occupied >90% of the field of view (10% was needed for reliable background estimation) or when the sheet started to touch the opposing side for the first time (the wound was partially closed). The mean distance advanced by the cell sheet was calculated from the wound edge traces at each time frame (one frame every 10 min), by the area difference between the sheet in the initial and current frame, and divided by the lateral y dimension of the field of view (wound closure is always in the x direction).

Nuclei detection

Nuclei of cells in the migrating cell sheets were detected using the H2B-mCherry fluorescent signals. Because the cells were densely packed, nuclei very often touched each other. A simple segmentation of the nuclei image would thus have yielded islands of nuclei that then would have to be further dissected into single nuclei by applying a watershed algorithm. Here, we used a complementary, very robust approach that did not require image segmentation. The intensity profile of an isolated nucleus was of cylindrical shape: an almost flat and circular intensity maximum that quickly decayed (edges with steep gradient) to background levels. The diameter of the intensity plateau was typically 10 pixels. Because the expression level of the histone marker varied from cell to cell, the intensity plateaus could have very different heights. Thus, the 1-d intensity profile of two neighboring nuclei looked like two consecutive step functions of different step heights. The gradient of such an intensity profile gave a strong response at the interface between the two nuclei, and this property was used here to dissect touching nuclei from each other. The gradient of the nuclei fluorescent image was calculated using a Sobel filter. This gradient image was then normalized to the intensity range of the raw nuclei image and subtracted from the latter. All pixel values that fell below background value because of the subtraction were set to background level. Comparison of the raw and gradient subtracted image showed that this procedure created an intensity rim between neighboring nuclei. To equalize the very different intensity maxima, we next applied a double logarithm of the processed image and then filtered with a broad Gaussian with a standard deviation of r = 5 pixels and subsequently applied a local maximum filter of circular support with r = 5 pixels to detect all local maxima in the image. We next applied a unimodal thresholding (Rosin, 2001) to the intensity histogram of the local maxima to cut off the local maxima in the background.

Confluent monolayers could not be analyzed with the Rosin algorithm because they did not contain the sufficient amount of background needed for this method to work properly. For these data, the threshold was determined by fitting a smooth spline to the intensity histogram of the local maxima. The threshold level was then set at the location of the first local minimum of the spline function. The rationale behind this approach was that the first local minimum in the histogram followed the first local maximum generated by maxima in the background. Thus, the first minimum in the spline function separated background from real signals. The obtained set of maxima corresponded to the nuclei positions.

The only weakness of this approach was the detection of nuclei shortly after cell divisions. The two daughter nuclei usually had higher fluorescent intensity and were smaller than the typical nuclei and thus generated high intensity gradients in the image. When subtracting this gradient, new daughter nuclei were often lost. Because these daughter nuclei were bright, they could easily be detected and added to the first set of nuclei by a second refinement step: We went back to the raw nuclei image and directly filtered it with a broad Gaussian of standard deviation r = 5 pixels and applied the local maximum filter (without taking the double logarithm). The Rosin method was again applied to the intensity histogram to cut off the maxima in the background. We now identified those maxima that were missed by the initial detection. These maxima had to fulfill an isolation criteria, which was that the distance to any already existing maximum from the initial detection had to be larger than 2× r = 10 pixels. Only those isolated maxima were added to the nuclei list, yielding the final result.

Nuclei tracking

The nuclei detection method yielded a point set of nuclei positions for each frame. Nuclei tracks were obtained by linking corresponding nuclei positions in consecutive frames using the single-particle tracking software described in Jaqaman et al. (2008). The underlying algorithm determines the optimal configuration of links between two point sets by minimizing the overall linking cost. The linking costs were calculated as the Euclidian distances between trajectory heads projected by Kalman filtering from the previous frame into the current frame and the actually detected nuclei of a frame (Jaqaman et al., 2008). To account for cell divisions and to repair broken tracks, the tracking algorithm also considers splitting events (but no merging) and performs a gap closing procedure. Only track segments with a length of at least three frames were considered for linking, and only gaps of maximum two frames were closed. All subsequent analyses were focused on cells with final tracks longer than 12 frames.

Spatial classification

Results from sheet edge and nuclei detection were combined to group the cells according to their distance to the wound edge. To this end, we calculated the Euclidean distance transform of the sheet mask. This transform assigns to each pixel in the black and white image its distance to the nearest zero pixel (a pixel in the wound). This distance map was then used to group cells into bands of equal relative distance to the wound edge. Measurements of speed, wound-directed velocity, persistence, velocity correlation, and normalized cell pair separation distance were plotted as functions of this relative distance to (or from) the wound edge. The chosen band widths were 250 pixels (~160 µm) for the persistence, normalized cell pair separation distance, and velocity correlation measurements and 100 pixels (~64 µm) for the other measurements. In some figures (Figs. 1 F and 2, C and F), measurements from multiple bands were plotted and denoted by "distance from wound edge."

Velocity, speed, and wound-directed velocity

Cell velocities were deduced from individual cell tracks. To reduce noise resulting from nuclei detection or stitching jitter, the velocity of cell *i* at time point t_j was defined as

$$\vec{v}_i\left(t_j\right) = \frac{\vec{x}_i\left(t_{j+6}\right) - \vec{x}_i\left(t_j\right)}{t_{j+6} - t_j},$$

in which $\vec{x}_i\left(t_j\right)$ is the position of cell *i* at frame *j*. Because frames were taken every 10 min, the moving mean defined in this paragraph had a time span of 1 h. From the velocity measurement, two migration properties plotted in the figures were calculated: speed and wound-directed velocity. The speed of cell *i* at time point *j* was calculated as the magnitude of its velocity $\left|\vec{v}_i\left(t_j\right)\right|$. Because the setup was designed such that wound healing always occurred along the x axis, the wound-directed velocity was given by the velocity's x component $v_{x,i}(t_j)$.

Persistence

The persistence of cell movement was defined as the ratio of the start to end point distance over the traversed path length:

$$P_{t_0,d}\left(t\right) = \left\langle \frac{\left|\vec{x}_i\left(t\right) - \vec{x}_i\left(t_0\right)\right|}{s_i\left(t_0, t\right)} \right\rangle.$$

Here, the traversed path length is given by

$$s_i\left(t_m, t_n\right) = \int_{t_m}^{t_n} \left|\dot{\vec{x}}_i\left(t'\right)\right| dt' = \sum_{k=m}^{n-1} \left|\vec{x}_i\left(t_{k+1}\right) - \vec{x}_i\left(t_k\right)\right|.$$

The mean in the first equation is taken over all cells *i* that, at time point t_0, were within a distance (d) in the interval $[d, d + \Delta d]$ from the wound edge, with Δd = 100 pixels (or ~64 µm). For ballistic motion, P = 1. Smaller values indicate nonpersistent, random motion.

Normalized cell pair separation distance measurement

Normalized cell pair separation distance quantified the divergence of initially neighbored cell tracks over time. Similar approaches had been used in nonlinear dynamics to study the sensitivity of trajectories on initial conditions (Strogatz, 1994). The equation we used is as follows:

$$M_{t_0,d}(t) = \left\langle \frac{R_{i,j}(t) - R_{i,j}(t_0)}{\frac{1}{2}\left(s_i(t_0,t) + s_j(t_0,t)\right)} \right\rangle_{R_{i,j}(t_0)<R_{\max}} . \quad (1)$$

The numerator measured the change of cell-to-cell distance $R_{i,j}(t) = \left|\vec{x}_i(t) - \vec{x}_j(t)\right|$ between the time points t_0 and t, as depicted in Fig. 2 A. To generate a measure that was insensitive to differences in cell speeds between conditions, we divided this numerator with the mean of the path lengths traversed by the two cells between t_0 and t,

$$s_i(t_0,t) = \int_{t_0}^{t} \left|\dot{\vec{x}}_i(t')\right| dt'$$

(Fig. 2 A). Numerically, Eq. 1 was evaluated by first finding all cells that were within a distance in the interval of $[d, d + \Delta d]$ from the wound edge, with Δd = 100 pixels (or ~64 µm). Then, we averaged over all cell pairs i,j that were initially separated by a distance of less than R_{max} = 50 pixels, or 32 µm, which was approximately the mean cell diameter. Thus, only pairs of nearest neighbor cells were considered in this analysis. A high normalized cell pair separation distance measurement indicates that the local neighborhood around the cells was quickly disrupted during cell movements, i.e., low coordination in cell movements. Also, note that this measurement is dimensionless and that it is closely related to the angle α between two diverging cell trajectories. For

$$\frac{R_{i,j}(t_0)}{R_{i,j}(t)} << 1$$

and approximate linear cell motion, it holds that $M/2 \approx \sin \alpha/2$. Unless otherwise noted (such as Fig. 2 C), all plots of normalized cell pair separation distance in the paper reflect measurements made starting 8 h after wounding (t_0) over a time course of 5 h for all neighboring cell pairs within 160 µm from the wound edge.

Velocity correlation

The velocity correlation between two cells was calculated by the following function:

$$C_{t,d}(R) = \frac{\left\langle \dot{\vec{x}}_i(t) \bullet \dot{\vec{x}}_j(t) \right\rangle}{\sqrt{\left\langle \dot{\vec{x}}_i(t)^2 \right\rangle \left\langle \dot{\vec{x}}_j(t)^2 \right\rangle}}, \forall \vec{x}_i \in \left[d, d + \Delta d\right] \cap \forall_{i,j} : R < \left|\vec{x}_i - \vec{x}_j\right| < R + \Delta R.$$

The function $C_{t,d}(R)$ measured the radial decay of the velocity correlation function at time point t for a cell at distance d from the wound edge. Here, R denoted the radial distance between the two cells i,j at positions $\vec{x}_i(t), \vec{x}_j(t)$ that moved with velocities $\dot{\vec{x}}_i(t), \dot{\vec{x}}_j(t)$ as depicted in Fig. 2 D. Numerically, this function was evaluated by first finding, at time point t, all cells i within a distance in the interval of $[d, d + \Delta d]$ from the wound edge with Δd = 250 pixels (or ~160 µm). For each cell within that group, we measured the pairwise distance to all other cells in the entire sheet and sorted them into radial bins $[R, R + \Delta R]$, with ΔR = 100 pixels (or ~64 µm). Then, we averaged over all pairings i,j in a radial bin according to the aforementioned equation. Unless otherwise noted (such as in Fig. 2 F), all plots of velocity correlation in the paper reflect measurements made for all cells 160 µm from the wound edge at 12 h after wounding.

Imaging and analysis of cell polarization

For measurement of cell Golgi orientations, MCF10A-H2B-mCherry cells were incubated with Golgi-GFP (CellLight; Invitrogen) following the manufacturer's instructions. Cells were then seeded for the constraint-removal wound-healing assays on PAA gel substrates. Fluorescent live-cell time-lapse imaging was performed as described in the section Fluorescent time-lapse imaging of cell migration, with additional acquisition of GFP signals at every third time point.

Unless otherwise noted, images acquired at 12 h after wounding were used to evaluate Golgi orientations during collective migration. Using the NIS-Elements software (Nikon), a vector was drawn from the center of the cell nucleus to the center of the Golgi-GFP signal for all cells expressing Golgi-GFP located at indicated distances or cell rows from the wound edge. These vectors represent the orientation of each cell's Golgi with respect to its associated nucleus. The angles between the drawn vectors and a vector pointing in the direction of wound healing were then recorded, reflecting Golgi orientations relative to the general direction of cell movements. The recorded angles were plotted in rose plots, or angle histogram plots, using MATLAB, in which the direction of each bar reflects the recorded angles, and the magnitude of each bar indicates the percentage of cells exhibiting those angles. Cells with Golgi orientations between 0 and 90° and between 270 and 0° were considered as having the Golgi anterior to the nucleus in the direction of wound healing. Cells with Golgi orientations between 90 and 270° were considered as having the Golgi posterior to the nucleus in the direction of wound healing. Between 34 and 429 cells from at least three independent experiments were analyzed for each plot. Statistical analyses were performed using Student's *t* tests, by evaluating whether the distributions of Golgi orientations were significantly different between the cell group of interest and cells located beyond 500 µm from the leading edge (which exhibited random Golgi orientation).

Imaging and analysis of lamellipodia or cryptic lamellipodia directionality

For measurements of lamellipodia or cryptic lamellipodia directionality, MCF10A cells stably expressing GFP-paxillin were mixed in a 1:10 ratio with unlabeled cells and seeded in wound-healing assays on PAA gel substrates. Wound healing was allowed to progress overnight, after which the collectively migrating cells were imaged using a spinning-disk confocal microscope. The imaging system consisted of a inverted motorized microscope (Ti-E) equipped with integrated Perfect Focus System, 40× Plan Apochromat 0.95 NA objective lens, a spinning-disk confocal head (CSU-X1; Yokogawa Corporation of America) with internal motorized high speed emission filter wheel and a Borealis modification (Spectral Applied Research) for increased light throughput and illumination homogeneity, a custom laser merge module (LMM-7; Spectral Applied Research) with acouto-optic tunable filters and 100–200-mW solid state lasers, a controller (ProScan II; Prior Scientific), a cooled charge-coupled device camera (ORCA-AG; Hamamatsu Photonics), and a custom-built 37°C microscope incubator enclosure with 5% CO_2 delivery. GFP fluorescence was excited with the 491-nm laser and collected with a quad 405/488/561/647-nm dichroic mirror (Semrock) and a 525/50-nm emission filter (Chroma Technology Corp.). Images were acquired with the MetaMorph image acquisition software (Molecular Devices) every 1.5 min for at least an hour, with the focal plane focused on the GFP-paxillin–labeled focal adhesions, allowing us to clearly identify the z section of the cells where the cells were in contact with the PAA gel surface and where the lamellipodia or cryptic lamellipodia protruded. Images were collected at multiple stage positions in each time loop, including at the leading edge of the migrating cell sheet, two fields of view (~250 µm) behind the leading edge, and four fields of view (~500 µm) behind the leading edge. The primary directions of lamellipodial or cryptic lamellipodial protrusion of the fluorescently labeled cells in each field of view were recorded from the time-lapse images. Between 34 and 78 cells were analyzed from at least three independent experiments for each distance from the wound edge.

Measurements of cellular pMLC levels

Immunostaining for pMLC was performed with the rabbit or mouse pMLC 2 (Ser19) antibody (Cell Signaling Technology) at 1:300 dilutions. Cells on PAA gel substrates were allowed to undergo wound healing overnight (15–20 h) before fixation with 4% PFA (Electron Microscopy Sciences) and permeabilization with 0.1% Triton X-100 (Thermo Fisher Scientific). Samples were incubated with the primary antibody for 1 h and probed with Alexa Fluor 488, 568, or 647 secondary antibodies, as well as DAPI to label nuclei and phalloidin to label actin, for 1 h. Samples were imaged with the laser-scanning confocal microscope (AIR; Nikon) with a 60× Plan Apochromat 1.4 NA objective lens and NIS-Elements acquisition software. DAPI and Alexa Fluor 488, 568, and 647 signals were excited with 404-, 488-, 561-, and 647-nm lasers, respectively, and collected through a quad 405/488/561/647-nm dichroic mirror and the 450/50-, 525/50-, 595/50-, and 700/75-nm emission filters, respectively. Z series optical sections at a step size of 0.35 µm were obtained at wound edge and multiple fields of view behind the leading edge. Laser intensity and exposure times were maintained at the same levels during all imaging sessions for each experiment. The mean protein

intensity per cell was calculated as the ratio of the background-subtracted total intensity in the z stack (sum over all pixels of slices) and the number of cells in the imaged region. The latter was obtained by manually counting cell nuclei in the maximum projected DAPI image. To compare across experiments, the mean pMLC intensity per cell values for each field of view were normalized to those of the wound edge cells taken during the same imaging session. To compare between different conditions, the normalized mean pMLC intensity per cell values were further normalized to those of control cells at the wound edge.

Analysis of cell spreading and cell heights

The mean spreading areas of leading edge cells on various substrate stiffnesses were measured using NIS-Elements software by hand drawing the outlines of leading edge cells and evaluating the resulting cell areas. Over 45 cells were analyzed from three independent experiments for each stiffness.

The mean cell heights on various substrate stiffnesses were evaluated from phalloidin and DAPI costains in z stacks acquired during confocal imaging of pMLC levels described in the previous section. At least 10 cells were randomly selected for measurement from images acquired from three independent experiments for each stiffness.

Measurement of focal adhesion sizes

To examine focal adhesion sizes in MCF10As undergoing collective migration, cells were seeded for wound healing on PAA gel substrates, and collective migration was allowed to progress overnight before cell fixation and permeabilization for immunofluorescence staining with antivinculin monoclonal antibody (V9264; Sigma-Aldrich) and anti–mouse Alexa Fluor 488, 568, or 647 secondary antibodies (Invitrogen). Images of focal adhesions at the sheet leading edge and multiple fields of view behind the sheet edge were acquired with the confocal microscope described in the section Imaging and analysis of lamellipodia or cryptic lamellipodia directionality using a 60× oil Plan Apochromat 1.4 NA objective lens. The lengths of focal adhesions were measured using the ImageJ software (National Institutes of Health).

Perturbation of cell–cell adhesions

The following siRNA SMARTpool reagents (Thermo Fisher Scientific) were used to knockdown cadherin-mediated cell–cell adhesions: P-cadherin or CDH3 (M-003823-00) and α-catenin or CTNNA1 (D-010505-03). siRNA transfection was performed as previously described (Simpson et al., 2008): In brief, ∼1.1 × 10^5 cells were transfected with 25 nM siRNA using the transfection reagent (DharmaFECT 3; Thermo Fisher Scientific). Experiments were conducted ∼48 h after transfection. Both mock transfected cells and cells transfected with nontargeting siRNA against luciferase (D-001100-01-20; Thermo Fisher Scientific) demonstrated no difference in any cell migration properties, including cell–cell coordination parameters compared with nontransfected MCF10A cells, and mock transfected cells were used as controls for all experiments. Cadherin-mediated cell–cell adhesions were also perturbed by expression of the dominant-negative E-cadherin construct pWZL-Blast-DN-Ecad (deposited in Addgene by the Weinberg laboratory; Onder et al., 2008). Knockdowns or expression of the proteins were validated by immunoblotting.

RNA interference of MIIA and MIIB

pLKO lentiviral small hairpin RNA (shRNA) vectors (Thermo Fisher Scientific) were used to down-regulate nonmuscle MIIA and MIIB (Iwanicki et al., 2011). MCF10As expressing E-cadherin–GFP were infected and selected with 1 µg/ml puromycin. Two shRNA vectors were tested separately per myosin isoform. For MIIA, sequences were as follows: sequence 1, 5′-CCGGGACAGCAATCTGTACCGCATTCTCGAGAATGCGGTACAGATTGCTGTCTTTTT-3′ (TRCN0000029466), and sequence 2, 5′-CCGGCCGCGAAGTCAGCTCCCTAAACTCGAGTTTAGGGAGCTGACTTCGCGGTTTTT-3′ (TRCN0000029467). For MIIB, sequences were as follows: sequence 1, 5′-CCGGGCACATATTCAGGACCTGGAACTCGAGTTCCAGGTCCTGAATATGTGCTTTTTG-3′ (TRCN0000123077), and sequence 2, 5′-CCGGGCAGCTAGTCTTGAGTCTCAACTCGAGTTGAGACTCAAGACTAGCTGCTTTTTG-3′ (TRCN0000123078). Knockdowns were confirmed by Western blotting. To achieve double knockdowns of MIIA with α-catenin, cells with stable shRNA knockdown of MIIA were transfected with siRNA against siCTNNA1 as described in the previous section.

Inhibitor reagents

Blebbistatin (Sigma-Aldrich) was used at a concentration of 25 µM, unless otherwise noted. Mitomycin C (Sigma-Aldrich) was used at a concentration of 1 ng/ml as in a previous study with MCF10A (Wrobel et al., 2004). Inhibitors were added immediately after removal of the PDMS block and before imaging.

Online supplemental material

Fig. S1 shows the schematic of the constraint-removal wound-healing assay as well as evidence demonstrating that the difference in wound healing of MCF10As on soft and stiff substrates is not dependent on the specific ECM protein used on cell proliferation but rather is the result of differences in cell spreading and translocation. Fig. S2 shows more detailed data supporting that cells undergoing collective migration respond to changes in substrate stiffness. Fig. S3 shows that substrate stiffness alters focal adhesion sizes and that the effects of substrate stiffness on collective migration properties is dependent on MIIA but less so on MIIB, likely because of the different functions or expression levels of the two isoforms in MCF10A cells. Fig. S5 shows that disrupting cell–cell adhesions alters focal adhesion sizes in cells undergoing wound healing and includes further evidence that the reduction in cell–cell coordination with weakened cell–cell adhesions can be partially rescued by low concentrations of blebbistatin. Video 1 shows 14-h progression of MCF10A collective migration on soft (3 kPa) and stiff (65 kPa) substrates. Video 2 shows tracking of H2B-mCherry–labeled nuclei in the migrating MCF10A cell sheets from Video 1 on soft (3 kPa) and stiff (65 kPa) substrates. Video 3 shows the lamellipodial and cryptic lamellipodial protrusion directions of cells undergoing collective migration. Video 4 shows that blebbistatin treatment reduces coordination during MCF10A wound healing. Video 5 shows the effects of disrupting cell–cell adhesions on collective migration properties, including the reduction in coordinated cell movements. Video 6 shows the partial rescue of coordinated migration by low, but not high, concentrations of blebbistatin. Online supplemental material is available at http://www.jcb.org/cgi/content/full/jcb.201207148/DC1.

We thank the Nikon Imaging Center at Harvard Medical School and its staff for assistance with microscopy. We further thank the Wyss Institute for Biologically Inspired Engineering and its staff for training and usage of the rheometer.

This project was supported by the Cell Migration Consortium (National Institutes of Health GM064346 to J.S. Brugge and G. Danuser), the Breast Cancer Research Foundation (to J.S. Brugge), and the Lee Jeans Foundation through the Entertainment Industry Foundation (to J.S. Brugge). M.R. Ng was supported in part by the National Institutes of Health Cell and Developmental Biology Training grant (GM07226). A. Besser was supported by the National Institutes of Health (grant R01 GM071868 awarded to G. Danuser) and the Deutsche Forschungsgemeinschaft fellowship (BE4547/1-1).

Submitted: 23 July 2012
Accepted: 24 September 2012

References

Alcaraz, J., R. Xu, H. Mori, C.M. Nelson, R. Mroue, V.A. Spencer, D. Brownfield, D.C. Radisky, C. Bustamante, and M.J. Bissell. 2008. Laminin and biomimetic extracellular elasticity enhance functional differentiation in mammary epithelia. *EMBO J.* 27:2829–2838. http://dx.doi.org/10.1038/emboj.2008.206

Arboleda-Estudillo, Y., M. Krieg, J. Stühmer, N.A. Licata, D.J. Muller, and C.-P. Heisenberg. 2010. Movement directionality in collective migration of germ layer progenitors. *Curr. Biol.* 20:161–169. http://dx.doi.org/10.1016/j.cub.2009.11.036

Block, E.R., and J.K. Klarlund. 2008. Wounding sheets of epithelial cells activates the epidermal growth factor receptor through distinct short- and long-range mechanisms. *Mol. Biol. Cell*. 19:4909–4917. http://dx.doi.org/10.1091/mbc.E08-01-0097

Block, E.R., A.R. Matela, N. SundarRaj, E.R. Iszkula, and J.K. Klarlund. 2004. Wounding induces motility in sheets of corneal epithelial cells through loss of spatial constraints: role of heparin-binding epidermal growth factor-like growth factor signaling. *J. Biol. Chem.* 279:24307–24312. http://dx.doi.org/10.1074/jbc.M401058200

Butcher, D.T., T. Alliston, and V.M. Weaver. 2009. A tense situation: forcing tumour progression. *Nat. Rev. Cancer*. 9:108–122. http://dx.doi.org/10.1038/nrc2544

Clark, K., M. Langeslag, C.G. Figdor, and F.N. van Leeuwen. 2007a. Myosin II and mechanotransduction: a balancing act. *Trends Cell Biol.* 17:178–186. http://dx.doi.org/10.1016/j.tcb.2007.02.002

Clark, R.A.F., K. Ghosh, and M.G. Tonnesen. 2007b. Tissue engineering for cutaneous wounds. *J. Invest. Dermatol.* 127:1018–1029. http://dx.doi.org/10.1038/sj.jid.5700715

Debnath, J., S.K. Muthuswamy, and J.S. Brugge. 2003. Morphogenesis and oncogenesis of MCF-10A mammary epithelial acini grown in three-dimensional basement membrane cultures. *Methods*. 30:256–268. http://dx.doi.org/10.1016/S1046-2023(03)00032-X

de Rooij, J., A. Kerstens, G. Danuser, M.A. Schwartz, and C.M. Waterman-Storer. 2005. Integrin-dependent actomyosin contraction regulates epithelial cell scattering. *J. Cell Biol.* 171:153–164. http://dx.doi.org/10.1083/jcb.200506152

Desai, R.A., L. Gao, S. Raghavan, W.F. Liu, and C.S. Chen. 2009. Cell polarity triggered by cell-cell adhesion via E-cadherin. *J. Cell Sci.* 122:905–911. http://dx.doi.org/10.1242/jcs.028183

Discher, D.E., P. Janmey, and Y.L. Wang. 2005. Tissue cells feel and respond to the stiffness of their substrate. *Science*. 310:1139–1143. http://dx.doi.org/10.1126/science.1116995

Doyle, A.D., F.W. Wang, K. Matsumoto, and K.M. Yamada. 2009. One-dimensional topography underlies three-dimensional fibrillar cell migration. *J. Cell Biol.* 184:481–490. http://dx.doi.org/10.1083/jcb.200810041

Dupin, I., E. Camand, and S. Etienne-Manneville. 2009. Classical cadherins control nucleus and centrosome position and cell polarity. *J. Cell Biol.* 185:779–786. http://dx.doi.org/10.1083/jcb.200812034

Edwards, K.A., and D.P. Kiehart. 1996. *Drosophila* nonmuscle myosin II has multiple essential roles in imaginal disc and egg chamber morphogenesis. *Development*. 122:1499–1511.

Engler, A., L. Bacakova, C. Newman, A. Hategan, M. Griffin, and D. Discher. 2004. Substrate compliance versus ligand density in cell on gel responses. *Biophys. J.* 86:617–628. http://dx.doi.org/10.1016/S0006-3495(04)74140-5

Engler, A.J., S. Sen, H.L. Sweeney, and D.E. Discher. 2006. Matrix elasticity directs stem cell lineage specification. *Cell*. 126:677–689. http://dx.doi.org/10.1016/j.cell.2006.06.044

Ewald, A.J., A. Brenot, M. Duong, B.S. Chan, and Z. Werb. 2008. Collective epithelial migration and cell rearrangements drive mammary branching morphogenesis. *Dev. Cell*. 14:570–581. http://dx.doi.org/10.1016/j.devcel.2008.03.003

Ewald, A.J., R.J. Huebner, H. Palsdottir, J.K. Lee, M.J. Perez, D.M. Jorgens, A.N. Tauscher, K.J. Cheung, Z. Werb, and M. Auer. 2012. Mammary collective cell migration involves transient loss of epithelial features and individual cell migration within the epithelium. *J. Cell Sci.* 125:2638–2654. http://dx.doi.org/10.1242/jcs.096875

Farooqui, R., and G. Fenteany. 2005. Multiple rows of cells behind an epithelial wound edge extend cryptic lamellipodia to collectively drive cell-sheet movement. *J. Cell Sci.* 118:51–63. http://dx.doi.org/10.1242/jcs.01577

Fenteany, G., P.A. Janmey, and T.P. Stossel. 2000. Signaling pathways and cell mechanics involved in wound closure by epithelial cell sheets. *Curr. Biol.* 10:831–838. http://dx.doi.org/10.1016/S0960-9822(00)00579-0

Firtel, R.A., and R. Meili. 2000. *Dictyostelium*: a model for regulated cell movement during morphogenesis. *Curr. Opin. Genet. Dev.* 10:421–427. http://dx.doi.org/10.1016/S0959-437X(00)00107-6

Flanagan, L.A., Y.E. Ju, B. Marg, M. Osterfield, and P.A. Janmey. 2002. Neurite branching on deformable substrates. *Neuroreport*. 13:2411–2415. http://dx.doi.org/10.1097/00001756-200212200-00007

Friedl, P., and D. Gilmour. 2009. Collective cell migration in morphogenesis, regeneration and cancer. *Nat. Rev. Mol. Cell Biol.* 10:445–457. http://dx.doi.org/10.1038/nrm2720

Friedl, P., P.B. Noble, P.A. Walton, D.W. Laird, P.J. Chauvin, R.J. Tabah, M. Black, and K.S. Zänker. 1995. Migration of coordinated cell clusters in mesenchymal and epithelial cancer explants in vitro. *Cancer Res.* 55:4557–4560.

Friedl, P., Y. Hegerfeldt, and M. Tusch. 2004. Collective cell migration in morphogenesis and cancer. *Int. J. Dev. Biol.* 48:441–449. http://dx.doi.org/10.1387/ijdb.041821pf

Ghosh, K., and D.E. Ingber. 2007. Micromechanical control of cell and tissue development: implications for tissue engineering. *Adv. Drug Deliv. Rev.* 59:1306–1318. http://dx.doi.org/10.1016/j.addr.2007.08.014

Guo, W.H., M.T. Frey, N.A. Burnham, and Y.L. Wang. 2006. Substrate rigidity regulates the formation and maintenance of tissues. *Biophys. J.* 90:2213–2220. http://dx.doi.org/10.1529/biophysj.105.070144

Gupton, S.L., and C.M. Waterman-Storer. 2006. Spatiotemporal feedback between actomyosin and focal-adhesion systems optimizes rapid cell migration. *Cell*. 125:1361–1374. http://dx.doi.org/10.1016/j.cell.2006.05.029

Hidalgo-Carcedo, C., S. Hooper, S.I. Chaudhry, P. Williamson, K. Harrington, B. Leitinger, and E. Sahai. 2011. Collective cell migration requires suppression of actomyosin at cell-cell contacts mediated by DDR1 and the cell polarity regulators Par3 and Par6. *Nat. Cell Biol.* 13:49–58. http://dx.doi.org/10.1038/ncb2133

Ilina, O., and P. Friedl. 2009. Mechanisms of collective cell migration at a glance. *J. Cell Sci.* 122:3203–3208. http://dx.doi.org/10.1242/jcs.036525

Ingber, D.E. 2006. Mechanical control of tissue morphogenesis during embryological development. *Int. J. Dev. Biol.* 50:255–266. http://dx.doi.org/10.1387/ijdb.052044di

Iwanicki, M.P., R.A. Davidowitz, M.R. Ng, A. Besser, T. Muranen, M. Merritt, G. Danuser, T.A. Ince, and J.S. Brugge. 2011. Ovarian cancer spheroids use myosin-generated force to clear the mesothelium. *Cancer Discov.* 1:144–157. http://dx.doi.org/10.1158/2159-8274.CD-11-0010

Jacob, M., and M. Unser. 2004. Design of steerable filters for feature detection using canny-like criteria. *IEEE Trans. Pattern Anal. Mach. Intell.* 26:1007–1019. http://dx.doi.org/10.1109/TPAMI.2004.44

Jaqaman, K., D. Loerke, M. Mettlen, H. Kuwata, S. Grinstein, S.L. Schmid, and G. Danuser. 2008. Robust single-particle tracking in live-cell time-lapse sequences. *Nat. Methods*. 5:695–702. http://dx.doi.org/10.1038/nmeth.1237

Keller, R. 2005. Cell migration during gastrulation. *Curr. Opin. Cell Biol.* 17:533–541. http://dx.doi.org/10.1016/j.ceb.2005.08.006

Knecht, D.A., and E. Shelden. 1995. Three-dimensional localization of wild-type and myosin II mutant cells during morphogenesis of *Dictyostelium*. *Dev. Biol.* 170:434–444. http://dx.doi.org/10.1006/dbio.1995.1227

Kolega, J. 2006. The role of myosin II motor activity in distributing myosin asymmetrically and coupling protrusive activity to cell translocation. *Mol. Biol. Cell*. 17:4435–4445. http://dx.doi.org/10.1091/mbc.E06-05-0431

Kostic, A., C.D. Lynch, and M.P. Sheetz. 2009. Differential matrix rigidity response in breast cancer cell lines correlates with the tissue tropism. *PLoS ONE*. 4:e6361. http://dx.doi.org/10.1371/journal.pone.0006361

Kuo, J.-C., X. Han, C.-T. Hsiao, J.R. Yates III, and C.M. Waterman. 2011. Analysis of the myosin-II-responsive focal adhesion proteome reveals a role for β-Pix in negative regulation of focal adhesion maturation. *Nat. Cell Biol.* 13:383–393. http://dx.doi.org/10.1038/ncb2216

Larsen, M., C. Wei, and K.M. Yamada. 2006. Cell and fibronectin dynamics during branching morphogenesis. *J. Cell Sci.* 119:3376–3384. http://dx.doi.org/10.1242/jcs.03079

Lee, P., and C.W. Wolgemuth. 2011. Crawling cells can close wounds without purse strings or signaling. *PLOS Comput. Biol.* 7:e1002007. http://dx.doi.org/10.1371/journal.pcbi.1002007

Levental, K.R., H. Yu, L. Kass, J.N. Lakins, M. Egeblad, J.T. Erler, S.F.T. Fong, K. Csiszar, A. Giaccia, W. Weninger, et al. 2009. Matrix crosslinking forces tumor progression by enhancing integrin signaling. *Cell*. 139:891–906. http://dx.doi.org/10.1016/j.cell.2009.10.027

Li, J., J. Chen, and R. Kirsner. 2007. Pathophysiology of acute wound healing. *Clin. Dermatol.* 25:9–18. http://dx.doi.org/10.1016/j.clindermatol.2006.09.007

Liu, Z., J.L. Tan, D.M. Cohen, M.T. Yang, N.J. Sniadecki, S.A. Ruiz, C.M. Nelson, and C.S. Chen. 2010. Mechanical tugging force regulates the size of cell-cell junctions. *Proc. Natl. Acad. Sci. USA*. 107:9944–9949. http://dx.doi.org/10.1073/pnas.0914547107

Lo, C.M., H.B. Wang, M. Dembo, and Y.L. Wang. 2000. Cell movement is guided by the rigidity of the substrate. *Biophys. J.* 79:144–152. http://dx.doi.org/10.1016/S0006-3495(00)76279-5

Macpherson, I.R., S. Hooper, A. Serrels, L. McGarry, B.W. Ozanne, K. Harrington, M.C. Frame, E. Sahai, and V.G. Brunton. 2007. p120-catenin is required for the collective invasion of squamous cell carcinoma cells via a phosphorylation-independent mechanism. *Oncogene*. 26:5214–5228. http://dx.doi.org/10.1038/sj.onc.1210334

Macri, L., and R.A. Clark. 2009. Tissue engineering for cutaneous wounds: selecting the proper time and space for growth factors, cells and the extracellular matrix. *Skin Pharmacol. Physiol.* 22:83–93. http://dx.doi.org/10.1159/000178867

Martin, P. 1997. Wound healing—aiming for perfect skin regeneration. *Science*. 276:75–81. http://dx.doi.org/10.1126/science.276.5309.75

Maruthamuthu, V., B. Sabass, U.S. Schwarz, and M.L. Gardel. 2011. Cell-ECM traction force modulates endogenous tension at cell-cell contacts. *Proc. Natl. Acad. Sci. USA*. 108:4708–4713. http://dx.doi.org/10.1073/pnas.1011123108

Matsubayashi, Y., M. Ebisuya, S. Honjoh, and E. Nishida. 2004. ERK activation propagates in epithelial cell sheets and regulates their migration during wound healing. *Curr. Biol.* 14:731–735. http://dx.doi.org/10.1016/j.cub.2004.03.060

Mori, H., N. Gjorevski, J.L. Inman, M.J. Bissell, and C.M. Nelson. 2009. Self-organization of engineered epithelial tubules by differential cellular motility. *Proc. Natl. Acad. Sci. USA*. 106:14890–14895. http://dx.doi.org/10.1073/pnas.0901269106

Murrell, M., R. Kamm, and P. Matsudaira. 2011. Substrate viscosity enhances correlation in epithelial sheet movement. *Biophys. J.* 101:297–306. http://dx.doi.org/10.1016/j.bpj.2011.05.048

Muschler, J., and C.H. Streuli. 2010. Cell-matrix interactions in mammary gland development and breast cancer. *Cold Spring Harb. Perspect. Biol.* 2:a003202. http://dx.doi.org/10.1101/cshperspect.a003202

Niewiadomska, P., D. Godt, and U. Tepass. 1999. *D*E-Cadherin is required for intercellular motility during *Drosophila* oogenesis. *J. Cell Biol.* 144:533–547. http://dx.doi.org/10.1083/jcb.144.3.533

Onder, T.T., P.B. Gupta, S.A. Mani, J. Yang, E.S. Lander, and R.A. Weinberg. 2008. Loss of E-cadherin promotes metastasis via multiple downstream transcriptional pathways. *Cancer Res.* 68:3645–3654. http://dx.doi.org/10.1158/0008-5472.CAN-07-2938

Paszek, M.J., N. Zahir, K.R. Johnson, J.N. Lakins, G.I. Rozenberg, A. Gefen, C.A. Reinhart-King, S.S. Margulies, M. Dembo, D. Boettiger, et al. 2005. Tensional homeostasis and the malignant phenotype. *Cancer Cell*. 8:241–254. http://dx.doi.org/10.1016/j.ccr.2005.08.010

Pelham, R.J., Jr., and Y. Wang. 1997. Cell locomotion and focal adhesions are regulated by substrate flexibility. *Proc. Natl. Acad. Sci. USA*. 94:13661–13665. http://dx.doi.org/10.1073/pnas.94.25.13661

Pelham, R.J., Jr., and Y.L. Wang. 1998. Cell locomotion and focal adhesions are regulated by the mechanical properties of the substrate. *Biol. Bull.* 194:348–349. http://dx.doi.org/10.2307/1543109

Peyton, S.R., and A.J. Putnam. 2005. Extracellular matrix rigidity governs smooth muscle cell motility in a biphasic fashion. *J. Cell. Physiol.* 204:198–209. http://dx.doi.org/10.1002/jcp.20274

Poujade, M., E. Grasland-Mongrain, A. Hertzog, J. Jouanneau, P. Chavrier, B. Ladoux, A. Buguin, and P. Silberzan. 2007. Collective migration of an epithelial monolayer in response to a model wound. *Proc. Natl. Acad. Sci. USA*. 104:15988–15993. http://dx.doi.org/10.1073/pnas.0705062104

Pouthas, F., P. Girard, V. Lecaudey, T.B.N. Ly, D. Gilmour, C. Boulin, R. Pepperkok, and E.G. Reynaud. 2008. In migrating cells, the Golgi complex and the position of the centrosome depend on geometrical constraints of the substratum. *J. Cell Sci.* 121:2406–2414. http://dx.doi.org/10.1242/jcs.026849

Prager-Khoutorsky, M., A. Lichtenstein, R. Krishnan, K. Rajendran, A. Mayo, Z. Kam, B. Geiger, and A.D. Bershadsky. 2011. Fibroblast polarization is a matrix-rigidity-dependent process controlled by focal adhesion mechanosensing. *Nat. Cell Biol.* 13:1457–1465. http://dx.doi.org/10.1038/ncb2370

Prasad, M., and D.J. Montell. 2007. Cellular and molecular mechanisms of border cell migration analyzed using time-lapse live-cell imaging. *Dev. Cell*. 12:997–1005. http://dx.doi.org/10.1016/j.devcel.2007.03.021

Reffay, M., L. Petitjean, S. Coscoy, E. Grasland-Mongrain, F. Amblard, A. Buguin, and P. Silberzan. 2011. Orientation and polarity in collectively migrating cell structures: statics and dynamics. *Biophys. J.* 100:2566–2575. http://dx.doi.org/10.1016/j.bpj.2011.04.047

Revenu, C., and D. Gilmour. 2009. EMT 2.0: shaping epithelia through collective migration. *Curr. Opin. Genet. Dev.* 19:338–342. http://dx.doi.org/10.1016/j.gde.2009.04.007

Ridley, A.J., M.A. Schwartz, K. Burridge, R.A. Firtel, M.H. Ginsberg, G. Borisy, J.T. Parsons, and A.R. Horwitz. 2003. Cell migration: integrating signals from front to back. *Science*. 302:1704–1709. http://dx.doi.org/10.1126/science.1092053

Rørth, P. 2009. Collective cell migration. *Annu. Rev. Cell Dev. Biol.* 25:407–429. http://dx.doi.org/10.1146/annurev.cellbio.042308.113231

Rosin, P.L. 2001. Unimodal thresholding. *Pattern Recognit.* 34:2083–2096. http://dx.doi.org/10.1016/S0031-3203(00)00136-9

Saez, A., M. Ghibaudo, A. Buguin, P. Silberzan, and B. Ladoux. 2007. Rigidity-driven growth and migration of epithelial cells on microstructured anisotropic substrates. *Proc. Natl. Acad. Sci. USA*. 104:8281–8286. http://dx.doi.org/10.1073/pnas.0702259104

Sakai, T., M. Larsen, and K.M. Yamada. 2003. Fibronectin requirement in branching morphogenesis. *Nature*. 423:876–881. http://dx.doi.org/10.1038/nature01712

Schwarz, U.S., N.Q. Balaban, D. Riveline, L. Addadi, A. Bershadsky, S.A. Safran, and B. Geiger. 2003. Measurement of cellular forces at focal adhesions using elastic micro-patterned substrates. *Mater. Sci. Eng. C-Biomimetic Supramol. Syst.* 23:387–394. http://dx.doi.org/10.1016/S0928-4931(02)00309-0

Simpson, K.J., L.M. Selfors, J. Bui, A. Reynolds, D. Leake, A. Khvorova, and J.S. Brugge. 2008. Identification of genes that regulate epithelial cell migration using an siRNA screening approach. *Nat. Cell Biol.* 10:1027–1038. http://dx.doi.org/10.1038/ncb1762

Small, J.V., T. Stradal, E. Vignal, and K. Rottner. 2002. The lamellipodium: where motility begins. *Trends Cell Biol.* 12:112–120. http://dx.doi.org/10.1016/S0962-8924(01)02237-1

Strogatz, S.H. 1994. Nonlinear dynamics and chaos: With applications to physics, biology, chemistry, and engineering. Addison-Wesley Publishing, Reading, Mass. 498 pp.

Tambe, D.T., C.C. Hardin, T.E. Angelini, K. Rajendran, C.Y. Park, X. Serra-Picamal, E.H. Zhou, M.H. Zaman, J.P. Butler, D.A. Weitz, et al. 2011. Collective cell guidance by cooperative intercellular forces. *Nat. Mater.* 10:469–475. http://dx.doi.org/10.1038/nmat3025

Trepat, X., M.R. Wasserman, T.E. Angelini, E. Millet, D.A. Weitz, J.P. Butler, and J.J. Fredberg. 2009. Physical forces during collective cell migration. *Nat. Phys.* 5:426–430. http://dx.doi.org/10.1038/nphys1269

Tse, J.R., and A.J. Engler. 2010. Preparation of hydrogel substrates with tunable mechanical properties. *Curr. Protoc. Cell Biol.* Chapter 10:Unit 10.16.

van Horssen, R., N. Galjart, J.A.P. Rens, A.M.M. Eggermont, and T.L.M. ten Hagen. 2006. Differential effects of matrix and growth factors on endothelial and fibroblast motility: application of a modified cell migration assay. *J. Cell. Biochem.* 99:1536–1552. http://dx.doi.org/10.1002/jcb.20994

Vasilyev, A., Y. Liu, S. Mudumana, S. Mangos, P.-Y. Lam, A. Majumdar, J. Zhao, K.-L. Poon, I. Kondrychyn, V. Korzh, and I.A. Drummond. 2009. Collective cell migration drives morphogenesis of the kidney nephron. *PLoS Biol.* 7:e9. http://dx.doi.org/10.1371/journal.pbio.1000009

Vitorino, P., and T. Meyer. 2008. Modular control of endothelial sheet migration. *Genes Dev.* 22:3268–3281. http://dx.doi.org/10.1101/gad.1725808

Vitorino, P., M. Hammer, J. Kim, and T. Meyer. 2011. A steering model of endothelial sheet migration recapitulates monolayer integrity and directed collective migration. *Mol. Cell. Biol.* 31:342–350. http://dx.doi.org/10.1128/MCB.00800-10

Weber, G.F., M.A. Bjerke, and D.W. DeSimone. 2012. A mechanoresponsive cadherin-keratin complex directs polarized protrusive behavior and collective cell migration. *Dev. Cell*. 22:104–115. http://dx.doi.org/10.1016/j.devcel.2011.10.013

Weijer, C.J. 2009. Collective cell migration in development. *J. Cell Sci.* 122:3215–3223. http://dx.doi.org/10.1242/jcs.036517

Williams, C.M., A.J. Engler, R.D. Slone, L.L. Galante, and J.E. Schwarzbauer. 2008. Fibronectin expression modulates mammary epithelial cell proliferation during acinar differentiation. *Cancer Res.* 68:3185–3192. http://dx.doi.org/10.1158/0008-5472.CAN-07-2673

Wozniak, M.A., R. Desai, P.A. Solski, C.J. Der, and P.J. Keely. 2003. ROCK-generated contractility regulates breast epithelial cell differentiation in response to the physical properties of a three-dimensional collagen matrix. *J. Cell Biol.* 163:583–595. http://dx.doi.org/10.1083/jcb.200305010

Wrobel, C.N., J. Debnath, E. Lin, S. Beausoleil, M.F. Roussel, and J.S. Brugge. 2004. Autocrine CSF-1R activation promotes Src-dependent disruption of mammary epithelial architecture. *J. Cell Biol.* 165:263–273. http://dx.doi.org/10.1083/jcb.200309102

Yeung, T., P.C. Georges, L.A. Flanagan, B. Marg, M. Ortiz, M. Funaki, N. Zahir, W. Ming, V. Weaver, and P.A. Janmey. 2005. Effects of substrate stiffness on cell morphology, cytoskeletal structure, and adhesion. *Cell Motil. Cytoskeleton*. 60:24–34. http://dx.doi.org/10.1002/cm.20041

Yin, J., K. Xu, J. Zhang, A. Kumar, and F.-S.X. Yu. 2007. Wound-induced ATP release and EGF receptor activation in epithelial cells. *J. Cell Sci.* 120:815–825. http://dx.doi.org/10.1242/jcs.03389